

## **General Disclaimer**

### **One or more of the Following Statements may affect this Document**

- This document has been reproduced from the best copy furnished by the organizational source. It is being released in the interest of making available as much information as possible.
- This document may contain data, which exceeds the sheet parameters. It was furnished in this condition by the organizational source and is the best copy available.
- This document may contain tone-on-tone or color graphs, charts and/or pictures, which have been reproduced in black and white.
- This document is paginated as submitted by the original source.
- Portions of this document are not fully legible due to the historical nature of some of the material. However, it is the best reproduction available from the original submission.

(NASA-CR-174166) FAR-INFRARED LINE EMISSION  
FROM THE GALAXY Ph.D. Thesis (Cornell  
Univ.) 225 p HC A10/MF A01 CSCL 03A

#85-13702

Unclas

63/89 24625

# CORNELL UNIVERSITY

*Center for Radiophysics and Space Research*

ITHACA, N. Y.

CRSR 823

FAR-INFRARED LINE EMISSION FROM THE GALAXY

Gordon John Stacey, Ph.D.

January 1985



**FAR-INFRARED LINE EMISSION**

**FROM THE GALAXY**

**A Thesis**

**Presented to the Faculty of the Graduate School**

**of Cornell University**

**in Partial Fulfillment of the Requirements for the Degree of**

**Doctor of Philosophy**

**by**

**Gordon John Stacey**

**January 1985**

Maril Harwit

## FAR-INFRARED LINE EMISSION FROM THE GALAXY

Gordon John Stacey, Ph.D.

Cornell University 1985

We have sampled the diffuse 157.74  $\mu\text{m}$  [CII] emission from the Galaxy at several galactic longitudes near the galactic plane including complete scans across the plane at  $l_{\text{II}} = 2.16^\circ$  and  $l_{\text{II}} = 7.28^\circ$ . The observed [CII] emission profiles follow closely the nearby  $^{12}\text{CO}$  ( $J=1+0$ ) emission profiles. The [CII] emission probably arises in neutral photo-dissociation regions near the edges of giant molecular clouds (GMC's). These regions have densities  $\sim 350 \text{ cm}^{-3}$  and temperatures  $T \sim 300^\circ\text{K}$ , and amount to  $\sim 4 \times 10^8 \text{ M}_\odot$  of hydrogen in the inner Galaxy. We estimate the total 157.74  $\mu\text{m}$  luminosity of the Galaxy to be  $\sim 6 \times 10^7 L_\odot$ . The volume filling factor of the [CII] emitting regions is  $\sim 10^{-3}$ .

We have also made estimates of the galactic emission in other far-infrared (FIR) cooling lines. We find the [CII] line to be the dominant FIR emission line from the galaxy and the primary coolant for the warm neutral gas near the galactic plane. Other FIR cooling lines predicted to be prominent in the galactic spectrum include the 51.82  $\mu\text{m}$  and 88.36  $\mu\text{m}$  fine structure lines of OIII and the 63.17  $\mu\text{m}$  and 145.53  $\mu\text{m}$  [OI] fine structure lines. The OIII lines are principal coolants for the ionized gas while the OI lines are significant coolants for the warm neutral gas.

We have also measured the 145.53  $\mu\text{m}$  [OI] emission line from the Orion Nebula with both a  $1'' \times 1''$  beam centered on the Trapezium and a  $7'' \times 7''$  beam encompassing most of the Orion Nebula. By comparing our measured 145.53  $\mu\text{m}$  intensity with previous measurements of the 63.17  $\mu\text{m}$  [OI] and 157.74  $\mu\text{m}$  [CII] intensities we determine that these three cooling lines all arise in the warm ( $T \sim 350^\circ\text{K}$ ) dense ( $n_H \sim 2.3 \times 10^5 \text{ cm}^{-3}$ ) carbon photodissociation region just beyond the ionization front separating the compact HII region from the molecular cloud. We find the 63.17  $\mu\text{m}$  radiation to be self-absorbed with line center optical depth  $\tau \sim 2$  and Doppler width (full-width-half-maximum)  $\sim 3.2 \text{ km s}^{-1}$ .

We have made these measurements using both NASA's Lear Jet facility and Kuiper Airborne Observatory (KAO). The Lear observations were made using a liquid helium cooled grating spectrometer which has been fitted with stressed Ge:Ga photoconductive detectors. This instrument is sensitive in the spectral range  $100 \mu\text{m} \lesssim \lambda \lesssim 195 \mu\text{m}$  with a spectral resolution  $R \equiv \lambda/\Delta\lambda \sim 200$ . For the KAO observations, we use a modified version of our grating spectrometer as an order sorter for our lamellar grating interferometer, with which we have achieved spectral resolutions in excess of 2000.

The analysis of the [CII] and [OI] lines presented in this thesis is a more sophisticated treatment of previous work which has appeared in the Astrophysical Journal (Stacey et al. 1983a,b and 1985).

**To my parents, for their constant encouragement and love.**

## ACKNOWLEDGMENTS

Many people have contributed to the success of my stay at Cornell and of this project. First and foremost is my thesis advisor, Prof. Martin Harwit. Martin's unique combination of talents, in both experimental and theoretical science has been a constant source of inspiration and guidance. Working with Martin has been an extremely rewarding experience at both professional and personal levels.

I would like to thank Professors James Cordes, Peter Gierasch and Saul Teukolsky for serving on my committee. They have provided sound advice on this and related projects, and critical readings of a previous draft of this document.

Technical advice and assistance has always been available from Dr. Terry Herter, George Gull and Prof. Jim Houck. The exchange of ideas between their lab and ours has contributed greatly to the success of this project.

I would also like to thank the ground and flight staffs of both the Kuiper Airborne Observatory and the Lear Jet Facility, for their excellent support. Special thanks to Steve Culp, Allan Meyer and Mike Robinson for their assistance in tight situations as we prepared for KAO flights and to Bob Mason for the special flight planning which led to our Lunar occultation measurements from the Lear. The navigators and pilots are to be thanked for their support and flexibility in the face of last minute flight plan alterations.

Barbara Boettcher drew all the figures in this thesis while Sylvia Corbin typed the versions of the work which have appeared in journals. Both are to be praised for their patience in the face of continual changes and last minute adjustments.

Noel Kurtz, Scott Smyers, Paul Viscuso and Chuck Fuller have all been co-conspirators in this project at one time or another. The first two were here when I arrived and the last two remain as I leave. It has been a pleasure to work with these people -- all of whom have proven to be good friends, an important consideration when one recalls the cramped quarters on the Lear Jet. Special thanks to Noel for ideas which eventually led to a greatly improved and simplified detector design.

It is with pleasure that I acknowledge membership in the CRSR Men's Club. To the Men's Club I owe softball and sailing in the summer, bowling and daiquiri parties in the winter and endless moments of bizarre entertainment all year round (e.g. liquid nitrogen bombs). Never shall I forget the proud softball teams with which I have played. The White Dwarfs, the Red Giants, the Quasi-Sober Objects, the Big Bangers and the Local Group -- we didn't win all the games, but we definitely had the most fun -- and drank the most beer.

Thanks to Paul Graf and Mark Shure who have been my office mates during most of my tenure at Cornell and also good friends. In times of despair and confusion, they could be relied on for the sound advice: "it just doesn't matter" (Mark) and "it only matters as much as you make it matter" (Paul). Paul was also my apartment-mate for the last three years -- I'm astounded we remained such good friends.

Dr. W. Reid Thompson typed the whole thesis and put it in the final form. "Dr. Reid" has been a good friend since the start of my adventure at Cornell. We have spent many evenings together pondering the complex mysteries of the universe while endeavoring to maximize our entertainment in our own small section thereof. I will always remember the late nights spent preparing this manuscript with Reid -- checking references, producing copy, and thinking profound thoughts while drinking the finest Milwaukee beverages and listening to the harmonious chords of the "B-52's".

My very special thanks go to Elizabeth Cameron, whose constant friendship, companionship, and affection during the last phases of this project kept life in perspective and made it all seem worthwhile. San Francisco, here we come!

Finally, I'd like to thank my parents Lindley Charles and DeAnn Atherton Stacey, who have always been there to share the times of triumph or despair, and whose constant love enabled them to resist placing me in an adoption home at an early age.

It is a pleasure to acknowledge financial support for this work from the taxpayers of America through NASA grants NSG 2347 and NGR 33-010-146.

## TABLE OF CONTENTS

Chapter/Section	Page
1 INTRODUCTION .....	1
2 INSTRUMENTS .....	7
.1 Introduction .....	7
.2 Inspiration .....	13
.3 Interferometer .....	18
.1 Theory .....	18
.2 The Fellgett Advantage .....	22
.3 Choosing Burst Size: The Nyquist Rate .....	26
.4 Functional Description .....	28
.5 Design Limitations .....	32
.4 Spectrometer .....	33
.1 Layout and Functional Description .....	33
.2 Optics .....	36
.3 Dewar .....	40
.4 Filters .....	41
.5 Electronics .....	44
.6 Stressed Detectors .....	48
.5 Aircraft Environments .....	54
.1 Lear Jet .....	54
.2 KAO .....	58
.6 Data Acquisition and Reduction .....	62
.1 Lear Jet .....	63
.2 KAO .....	68
3 FINE STRUCTURE LINES AND RADIATIVE TRANSFER .....	71
.1 Introduction .....	71
.2 Radiative Transfer .....	74

.1	Equation of Transfer .....	74
.2	Einstein Coefficients and Detailed Balance .....	77
.3	Optically Thin Lines .....	83
.4	Optically Thick Lines .....	93
.5	The Eddington Approximation .....	102
.6	Solution for a Plane Parallel Medium .....	104
.3	Cooling of the Interstellar Medium .....	106
.1	HII Regions .....	107
.2	Atomic Clouds .....	110
.3	Dense Molecular Clouds .....	113
.4	Cooling Through Gas-Grain Collisions .....	114
4	FAR INFRARED EMISSION LINE COOLING OF THE GALAXY .....	116
.1	Introduction .....	116
.1	Importance of C <sup>+</sup> .....	116
.2	History of Observations of the [CII] line .....	117
.3	Diffuse Matter in the Galaxy .....	121
.2	The Diffuse 157 $\mu$ m [CII] Emission of the Galaxy .....	124
.1	Introduction .....	124
.2	Modus Operandi .....	126
.1	Lunar occultation .....	126
.1	Techniques .....	126
.2	Results .....	131
.2	Contour tracing through beam switching .....	135
.1	Reconstruction of [CII] contours .....	136
.2	Results .....	138
.3	Discussion .....	141
.1	The Ionized Gas .....	141
.2	The Neutral Gas .....	145
.1	CII regions .....	145
.2	CII opacity .....	148
.3	CII Luminosity of the Galaxy .....	150
.4	Heating of CII Regions .....	152
.1	Cosmic rays .....	152
.2	Photodissociation of H <sub>2</sub> .....	153
.3	Photoionization of heavy elements .....	154

.4	Photoelectric emission from grains .....	154
.5	Comparison with the Results of Pottasch, Wesselius and van Duinen .....	156
.6	Estimates of other FIR Spectral Line Emission from the Galaxy .....	157
.1	Dense molecular clouds .....	158
.2	CII regions .....	159
.3	Atomic gas .....	160
.4	Ionized gas .....	163
.7	The 8° Region .....	164
.4	Continuum Measurements .....	168
.5	Summary .....	170
5	[OI] EMISSION FROM THE ORION NEBULA .....	171
.1	An Overview of the Orion Nebula .....	171
.2	Introduction .....	174
.3	Observations .....	175
.1	145.53 $\mu$ m Observations .....	175
.1	KAO observations .....	175
.2	Lear observations .....	177
.2	63.17 $\mu$ m Observations .....	177
.4	Discussion .....	179
.1	Ionization Fronts .....	181
.2	Warm Neutral Regions .....	182
.1	Broadbeam models .....	182
.2	Trapezium region model .....	188
.5	Summary .....	191
	APPENDIX: SELECTED FAR INFRARED FINE STRUCTURE TRANSITIONS ...	192
	REFERENCES .....	196

## LIST OF TABLES

Table	Page
3.1. Critical Densities of [OI] and [CII] Transitions .....	86
3.2. Ionization Potentials and Excitation Temperatures of the Abundant Heavy Elements .....	109
4.1. Other 157 $\mu\text{m}$ [CII] Observations .....	120
4.2. Dates, Times and Galactic Coordinates of Lunar Observations .....	129
4.3. Intensities for Galactic CII Emission from Lunar Occultation Measurements .....	133
4.4. Galactic [CII] Line Intensities .....	142
4.5. Expected Far Infrared Emission Lines from the Inner Galaxy .....	165
5.1. Far Infrared Fine Structure Lines Observed in Orion .....	173
5.2. Observations .....	180
5.3. Models .....	190

## LIST OF FIGURES

Figure	Page
2.1. Detection of the J=16→15 Rotational Transition of CO in Orion .....	25
2.2. Schematic of Lamellar Grating Interferometer .....	29
2.3. Apodization of an Interferogram .....	34
2.4. Detection of the J=17→16 Rotational Transition of CO in Orion .....	35
2.5. Schematic of Liquid Helium Cooled Spectrometer .....	37
2.6. Comparison of FIR Reststrahlen Filters .....	43
2.7. Circuit Diagram for Transimpedance Amplifier .....	45
2.8. Stressed Detector Housing Design .....	51
2.9. Theoretical FIR Spectrum of Jupiter .....	67
3.1. Energy Level Diagram for Neutral Oxygen .....	73
3.2. Relative Level Populations of C <sup>+</sup> vs. n <sub>e</sub> , n <sub>HI</sub> and n <sub>H<sub>2</sub></sub> ....	87
3.3. Reduced Emissivity of C <sup>+</sup> vs. n <sub>e</sub> , n <sub>HI</sub> and n <sub>H<sub>2</sub></sub> .....	89
3.4. Relative Level Populations of OI vs. n <sub>HI</sub> .....	91
3.5. Relative Level Populations of OI vs. n <sub>e</sub> .....	92
3.6. Reduced Emissivity of OI vs. n <sub>HI</sub> .....	94
3.7. Reduced Emissivity of OI vs. n <sub>e</sub> .....	95
3.8. Ratio of 63.17 μm to 145.53 μm Line Intensities vs. n <sub>e</sub> and n <sub>HI</sub> .....	96
3.9. [CII] and [OI] Cooling for Neutral Clouds .....	112
4.1. Position of Moon During Lunar Occultation Scan .....	130
4.2. [CII] Emission Measured with Lunar Occultation Scan .....	134
4.3. Observing Positions for Contour Tracing Technique .....	139
4.4. Galactic 157.74 μm [CII] Spectra .....	140
4.5. [CII] Intensity at Three Galactic Latitudes .....	143
4.6. [CII] Scans Superposed on Nearby <sup>12</sup> CO Scans .....	149
4.7. Ratio of the (157 μm) [CII] to (63 μm) [OI] Line Intensities vs. n <sub>HI</sub> .....	161
4.8. 157 μm Continuum Scans .....	169

5.1.	145.53 $\mu\text{m}$ Fourier Transform Spectrum of the Trapezium ...	176
5.2.	145.53 $\mu\text{m}$ Grating Spectrum of the Orion Nebula .....	178
5.3.	Ratio of the (145 $\mu\text{m}$ ) [OI] to (157 $\mu\text{m}$ ) [CII] Line Intensities vs. $n_{\text{HI}}$ .....	185

"We changed again, and yet again, and now it was too late and too far to go back, and I went on. And the mists had solemnly risen now, and the whole world lay spread before me."

Pip- in Charles Dickens' Great Expectations

## CHAPTER 1

### INTRODUCTION

The far-infrared (FIR) may be loosely defined as those wavelengths in the electromagnetic spectrum lying between 20 and 300  $\mu\text{m}$ . Spectroscopic work done at wavelengths beyond 300  $\mu\text{m}$ , often termed "submillimeter", is distinguished from FIR spectroscopy, in that submillimeter radiation is usually detected with coherent techniques, analogous to heterodyne receivers in use in modern radio astronomy. In contrast, until very recently, most spectroscopy done in the FIR has been done with incoherent devices in combination with optical filtering techniques. Instruments in current use for FIR spectroscopy include grating spectrometers, Fabry-Perot interferometers, Michelson interferometers and the lamellar grating interferometer discussed in this thesis. The various devices have their advantages and disadvantages which we discuss in Chapter 2.

There is a wealth of astronomical information to be gained through studies in the FIR. The FIR is unique in several respects:

- 1) Objects as different as planets and quasars emit the bulk of their radiant energy in the FIR, and show the peak of their spectral emission at wavelengths longward of 20  $\mu\text{m}$ .

2) The FIR is unhindered by the extinction problems which plague the optical and near infrared astronomers. Typical grain sizes in the general interstellar medium (ISM) are  $\sim .1 \mu\text{m}$  so the Galaxy is virtually transparent to FIR radiation. Regions totally obscured to optical observers, such as the galactic center, are accessible to FIR experimenters.

3) The FIR is filled with emission lines produced through collisional excitation of atoms, ions and molecules with low-lying energy states. These lines are usually optically thin, and have excitation temperatures  $30^\circ \lesssim T \lesssim 600^\circ\text{K}$ . Thus, these lines are sensitive temperature probes in the intermediate temperature regimes associated with low-velocity shock or ionization fronts or warm neutral gas. The optical lines are not excited in such low temperature regimes, while the radio emitting levels are largely populated according to their statistical weights and are therefore insensitive to temperature.

4) In high temperature ionized gas regions, the FIR emitting level populations are temperature insensitive and determined primarily by the densities in the emitting regions (Chapter 3). The FIR lines provide excellent density probes for these regions.

Unfortunately, the Earth's atmosphere is largely opaque in the FIR due to the omnipresent molecule,  $\text{H}_2\text{O}$ . However, the column density of water vapor declines dramatically with increasing altitude, decreasing by a factor of  $\sim 500$  as one ascends from mountaintop altitudes (4.2 km) to aircraft altitudes (14 km) (Traub and Stier 1976). Thus, one is able to pursue sensitive observations in the FIR from NASA's two airborne observatories, the Lear Jet facility and Kuiper Airborne Observatory (KAO).

The Lear Jet is the smaller of these two observatories, containing a 30 cm f/6.5 telescope mounted in an open port in the airplane's fuselage. The power incident on detectors from an infrared source whose angular extent,  $\Omega_S$ , is greater than the telescope beam,  $\Omega_T$ , is proportional to  $A\Omega_T$  where A is the surface area of the telescope primary mirror. The second law of thermodynamics requires that this product be a constant for any diffraction limited telescope regardless of aperture size. Thus, for diffuse emission regions, the light gathering power of the Lear Jet telescope is the same as that for the much larger telescope aboard the KAO. Furthermore, the larger chopper throw of the Lear Jet permits observations of more extended regions (see Section 2.1). Thus, for observations of extended sources of emission (e.g. galactic plane observations -- see Chapter 4) we use the Lear Jet facility.

For sources of angular extent,  $\Omega_S$ , smaller than the telescope beam size,  $\Omega_T$ , the power incident on our detectors is proportional to  $A\Omega_S$ . Thus, for sources which do not fill the  $4'' \times 7''$  beam of the Lear Jet, the 91 cm telescope aboard the KAO has up to ten times the light gathering power of the Lear telescope. The KAO is a much larger facility (being a modified C141A Starlifter) and thus may accommodate a host of experimenters and crew in addition to larger instrument packages on the telescope. Therefore, for high spatial resolution ( $\sim 1'' \times 1''$ ) measurements, or for measurements of point sources, we use the KAO facility.

Observations reported in this work come from both the Lear Jet and KAO facilities. Lear Jet observations were made with a liquid helium cooled grating spectrometer, which is essentially an improved version of

the spectrometer first described by Houck and Ward (1979). We have installed stressed Ge:Ga detectors in this system which gives us sensitivity in the spectral range  $100 \mu\text{m} \leq \lambda \leq 195 \mu\text{m}$ . We have also improved system sensitivity through the implementation of new detector designs and manufacturing techniques and the installation of low noise J-FETs in the first stage electronics.

The additional space available aboard the KAO allows us to employ a lamellar grating interferometer for our KAO observations. We use the grating spectrometer as an order sorter for the resolution achieving interferometric stage. The spectrometer used for KAO observations is identical to that used for Lear observations except that the f/6.5 Lear optics have been replaced with f/17 optics to match the beam of the KAO (Meinick 1981). Our instruments are described in detail in Chapter 2.

The first astronomical detection of a FIR fine structure line was the observation of the  $88 \mu\text{m}$  [OIII] line emanating from the M17 (Ward et al. 1975). Since then, a host of FIR fine-structure and molecular rotational transitions have been observed in emission and absorption from interstellar clouds. A compendium of FIR fine structure lines is presented in the Appendix.

The FIR fine structure lines arise in atoms with 1, 2, 4, or 5 equivalent p electrons. The spin-orbit (L-S) interaction splits terms of total spin, S, and total orbital angular momentum, L, into a set of fine structure levels, each of which represents a different value for the total angular momentum vector J, determined by the vector addition of L and S. Since transitions among states of different J involve no change in the electronic spin or orbital angular momentum, they are forbidden to

electric dipole radiation. Magnetic dipole transitions, however, are allowed, and as such the excited states are metastable with lifetimes of the order of days. The excited levels may thus be collisionally depopulated in dense ( $n_{\text{HI}} \gtrsim 10^5 \text{ cm}^{-3}$ ) regions. We discuss the physics of fine structure line emission and radiative transport in interstellar clouds in Chapter 3.

Since the FIR fine-structure lines are generally optically thin and collisionally excited at low densities, they serve as excellent coolants for the general ISM (see Section 3.3). The dominant coolants for warm ( $T \gtrsim 70^\circ\text{K}$ ) low density ( $n_{\text{H}} \lesssim 10^6 \text{ cm}^{-3}$ ) neutral clouds are the fine structure lines of the astrophysically abundant species CII and OI. As collapsing clouds must go through these temperature and density ranges when forming protostars, studies of the [CII] and [OI] lines in star formation regions should lead to a better understanding of how stars are formed from interstellar gas. We have measured the  $^3\text{P}_0 - ^3\text{P}_1$  (145.53  $\mu\text{m}$ ) [OI] transition in the Orion Nebula, believed to be a region of active star formation. In Chapter 5, we incorporate this measurement with previous measurements of the  $^3\text{P}_{3/2} - ^3\text{P}_{1/2}$  (157.74  $\mu\text{m}$ ) [CII] fine structure line to build a model for the warm neutral regions just outside the ionization front in Orion.

The primary thrust of this work, the measurement of the 157  $\mu\text{m}$  [CII] emission from the Galaxy is contained in Chapter 4. Most of the mass in the galactic interstellar medium is contained within atomic or molecular hydrogen clouds. Neutral clouds near the galactic plane are probably enveloped in warm ( $T \sim 300^\circ\text{K}$ ) low density ( $n_{\text{HI}} \lesssim 10^3 \text{ cm}^{-3}$ ) "CII"

regions generated by the ionizing effects of the interstellar radiation field (see Section 4.3). The dominant cooling transition for these warm neutral regions is the [CII] fine structure line at 157.74  $\mu\text{m}$ , with a lesser contribution from the 63.17  $\mu\text{m}$  [OI] line. We have sampled diffuse [CII] emission from the Galaxy at several galactic longitudes including complete scans at  $l^{\text{II}} = 2.16^\circ$  and  $l^{\text{II}} = 7.28^\circ$ . These measurements allow us to deduce that the [CII] emission arises predominantly from the edges of giant molecular clouds within the solar circle and that there are knotlike features in the [CII] emission. We are able to estimate temperatures and densities in the emitting regions and estimate the [CII] luminosity and the total [CII] emitting mass of the Galaxy. We also predict the galactic luminosity of other FIR and submillimeter emission lines. We conclude that the [CII] line is the dominant FIR emission line in the Galaxy and the primary coolant for the warm neutral gas.

## CHAPTER 2

### INSTRUMENTS

#### 2.1. Introduction.

The primary design consideration for any FIR spectrometer is the detection of the maximum number of astrophysically interesting spectral lines in the minimum time. Detection of these lines is hampered by the fact that the atmosphere, being a good absorber of infrared photons, is also a copious emitter of infrared photons. In addition to this "sky" background the telescope and telescope cavities are also good infrared emitters, adding to the background flux. Let us investigate the nature of this background.

If we assume the background emitters behave like a graybody of emissivity  $\epsilon_v$  at temperature,  $T$ , then the total number of background photons at frequencies,  $\nu$ , absorbed by the detector per unit time, in frequency interval  $d\nu$  is:

$$N_\nu = \tau_\nu \eta_\nu B_\nu \epsilon_\nu A \Omega \, d\nu / h\nu$$

where

$B_\nu$  = Planck blackbody function;

$\eta_\nu$  = quantum efficiency of the detector, i.e.,

# photons absorbed  $\div$  # photons incident on the detector;

$\tau_v$  = transmission of helium cooled optics;

$A\Omega$  = aperture - solid angle product of the optical system (in the ideal, diffraction limited case

$$A\Omega = 3.7 \lambda^2 \text{ cm}^2 \text{ sr};$$

$h$  = Planck's constant.

In terms of the system resolution,  $R \equiv v/dv$  we have

$$N_v = n_v \tau_v \epsilon_v B_v A\Omega / hR$$

For the present calculation, we assume  $\epsilon_v$  is given roughly by the emissivity of the sky at  $150 \mu\text{m}$  and at aircraft altitude of  $41,000'$ ;  $\epsilon_v = .25$  (Traub and Stier 1976). Taking a "typical" transmission for a grating spectrometer  $\tau_v \sim .3$ , detector quantum efficiency  $n_v = .15$ , and a sky temperature  $T \sim 250^\circ\text{K}$  we have:

$$N_v \sim (4 \times 10^{11}) / R \text{ photons/sec}$$

If we let  $R = 200$  we will have  $N_v \sim 2 \times 10^9$  photons/sec. In contrast, from an especially strong continuum source at  $150 \mu\text{m}$  we might detect  $\sim 10^8$  photons/sec at this resolution, and from a strong line at this wavelength we might detect  $2 \times 10^7$  photons/sec. Thus, we are faced with the problem of detecting source radiation which is at least a factor of 50 weaker than the background radiation. The procedures generally employed to compensate for this large thermal background are called "chopping" and "nodding". The Cassegrain telescope secondary mirrors on both the Lear Jet and KAO are designed to wobble in a square

wave pattern thus causing the beam alternately to look at two portions of the sky. If one places the FIR source in one of the two beams, the result will be an oscillating photon flux at the detector due to the source, on top of a large D.C. offset due to the thermal background. This procedure is called "chopping" and the two beams are often referred to as "plus" beam and "minus" beam. Unfortunately, it is nearly always the case that one side of the telescope cavity is warmer than the other. Thus, the thermal background may be larger in one beam than in the other. There might also be a gradient in the sky background. These gradients in the thermal background will then give rise to an A.C. signal. To compensate for this second order effect, one uses the procedure called "nodding", i.e., first integrating with the source in the plus beam for a certain integration time (usually ~ 5 seconds) and then integrating again with the source in the minus beam. The difference between these integrations will then give twice the signal due to the source and effectively eliminate first order thermal gradients.

The above procedures enable us to distinguish a small source signal in the presence of a large thermal background. Unfortunately, these procedures do not eliminate the noise associated with this background flux.

In the most optimistic case, the noise in the background flux is due to the statistical fluctuations in photon arrival rates. If we let  $N_b$  = number of background photons absorbed by our infrared detector as above, then the RMS fluctuations in the photon flux is given by (Boyd 1982)

$$\Delta N_{\nu} = [ 2N_{\nu}(1+n_{\nu}\bar{n}_{\nu})/\Delta t ]^{1/2}$$

where  $\bar{n}_{\nu} \equiv 1/(e^{h\nu/kT}-1)$  is the photon occupancy and  $\Delta t$  is the integration time. The first term in parentheses is the classical "shot noise" due to the discrete arrival rate of photons. The second purely quantum mechanical term is often referred to as "excess noise" and is due to photon bunching. Due to the Bose-Einstein nature of the radiation field the mean number of photons per field mode is greater than unity. For  $T \sim 250K$  at  $150 \mu m$ ,  $\bar{n} \sim 2.1$ .

In terms of the system parameters resolution,  $R$ , and throughput  $T_{\nu} \equiv \tau_{\nu}n_{\nu}$  the fluctuations seen by the system at  $150 \mu m$  are

$$\Delta N_{\nu} \sim 5 \times 10^5 (T_{\nu}/R)^{1/2}$$

Thus, one may reduce the background fluctuations by increasing system resolution, or decreasing system throughput. Obviously one does not wish to minimize the fluctuations by decreasing system throughput as the signal strength is proportional to  $T_{\nu}$  and the photon noise is only proportional to  $T_{\nu}^{1/2}$ . Therefore, the way to decrease system noise, when the system noise is dominated by photon noise, is to increase system resolution.

With recent developments in crystal growth and electrical contact-implantation techniques, infrared detectors are now available whose intrinsic noise is much less than the photon noise above. Johnson noise may be reduced through suitable selection of load resistors and amplifiers are also available whose intrinsic noise is much less than the photon noise. One should, then, be able to achieve photon-noise-limited performance in an aircraft environment. Generally, however, it is found

that background fluctuations are a factor of 5 or 10 larger than those due to photon noise. The cause of this excess noise is probably a combination of changing airmasses, fluctuating sky emissivity and temperature, or atmospheric turbulence inside and outside of the telescope cavity. However, the conclusion remains: higher system resolution should result in smaller background noise. For discussions of background-limited performance in the FIR, see Keyes and Quist (1970), Gillett, Dereniak and Joyce (1977), and Boyd (1982).

Increasing system resolution is beneficial in other respects also.

1) Many FIR spectral lines are formed in regions which also have high continuum flux levels due to thermal emission from interstellar dust. Until one actually resolves a line, higher spectral resolution will enhance the presence of a line at the expense of the continuum. This is important as the system response is a convolution of many functions which vary from one wavelength to another. Included are the spectrometer response function, filter transmission functions, atmospheric transmission and beam profile. Much of this problem is alleviated through dividing the source spectrum by a suitable calibrator spectrum which is presumed to emit like a blackbody (see Section 2.6). However, false spectral features may still persist. These may be caused by different solid angles being subtended by the source and calibrator tending to alter the instrumental profile; wavelength calibration errors due to pointing errors; different airmasses through which the source and calibrator were observed or even spectral features in the calibrator spectrum itself. These problems are minimized through the use of a high resolution spectrometer which need only observe the continuum immediately adjacent to the interstellar spectral feature.

A good example of calibration problems is the  $63.17 \mu\text{m}$  [OI] line which is located on the wing of a very deep telluric water vapor absorption feature only  $\sim .15 \mu\text{m}$  away. If the resolution of the spectrometer used to measure the OI feature is only moderate ( $\lambda/\Delta\lambda \sim 200$ ), the water vapor and [OI] features are not distinguished by the spectrometer. Hence, it is necessary to obtain a calibration spectrum whose wavelength scale is precisely that of the source spectrum and in which the water vapor feature is saturated to the same degree as the source spectrum. In practice, this is not easy to do and large calibration errors may remain. If the saturation of the water feature is higher in the calibrator, the divided spectrum might show an emission feature to appear at  $63.17 \mu\text{m}$  even if the source had no such feature! Higher spectral resolution eliminates much of this problem.

2) A second reason that high resolution is desirable is that when an interstellar line is actually resolved, one may infer from the line width bulk physical properties of the emitting region such as turbulent velocities, or if the broadening is thermal, kinetic temperature.

3) Lastly, the FIR spectrum of many regions is so thick with spectral lines, that one needs high resolution to separate and correctly identify spectral features. A good example of this is the BN-KL region in Orion where we have recently discovered the  $163.124 \mu\text{m}$  and  $163.397 \mu\text{m}$  emission lines of excited OH (Viscuso et al. 1985). These lines are immediately adjacent to the previously measured  $162.812 \mu\text{m}$ ,  $J = 16-15$  rotational transition of shocked CO. If the resolution of our instrument had been less than  $\sim 500$ , it would have been impossible to distinguish these features.

In some cases, astrophysically interesting species have transition wavelengths which are not precisely known. Such species may be difficult to produce in the lab, or may have excited levels from which radiative transitions are preempted by collisional de-excitation. Furthermore, the level energies may be difficult to precisely calculate quantum mechanically, hence, the most accurate energy level diagrams for such a species may be drawn from astrophysical measurements of the transition frequencies. .

## 2.2. Inspiration.

There are two categories of high resolution incoherent detection techniques in current use in the FIR. The first group, referred to as monochromators, samples one spectral resolution element at a time and includes such instruments as grating spectrometers and Fabry-Perot (FP) spectrometers. The second group includes multiplexing spectrometers such as Michelson interferometers or lamellar grating spectrometers. These instruments sample a number of independent spectral elements simultaneously and recover the power spectrum through Fourier transform techniques. We refer to these as FTS (Fourier transform spectro-

grapher) spectrometers. A real spectrometer would have variable resolution so that one could resolve lines when one wishes to measure line intensities or over-resolve a line when one wishes to obtain Doppler width or Doppler shift information. Narrow FIR lines have line widths less than 1 km/sec, corresponding to a resolution  $> 3 \times 10^5$ , so one might consider construction of an instrument with such resolution. In practice, such an instrument is quite difficult to construct. A more reasonable design

goal would be  $R \sim 10^4$  at which transitions such as the lines due to shocked CO in the BN-KL region of the Orion Nebula would be just resolved and diffuse emission lines from extragalactic sources would be over-resolved.

The most straightforward technique for achieving high resolution is the construction of a grating spectrometer. The first FIR lines from astronomical sources were discovered with such devices. Given background limited detection and plenty of work space, such an instrument is probably more useful than a FP or FTS. A well-designed grating spectrometer may have a throughput approaching 40%, while our own FTS is only  $\sim 17\%$  efficient and good FP systems pass only 10-15% of the radiation incident upon them (Watson 1982). Furthermore, a grating instrument is often readily tunable over a continuous range of wavelengths. For example, our medium resolution spectrometer is continuously tunable from  $\sim 100$  to  $200 \mu\text{m}$  in first order, and may be used from  $\sim 55 \mu\text{m}$  -  $200 \mu\text{m}$  if one of the two detectors operates in the second order of the grating. Finally, a grating monochromator permits the use of many detectors in the focal plane along the direction of the dispersion of the grating. It is not unusual for a grating spectrometer to have 10 detectors in the focal plane leading to a net sensitivity gain of  $\sqrt{10}$  over a FP instrument of the same resolution which typically may illuminate just one detector. However, a simple grating instrument with  $R \sim 10^4$  would require a grating  $\sim 75$  cm long. Such an instrument would be difficult to install on the KAO much less be kept helium cooled. (On the Lear Jet such a grating would protrude through the fuselage.)

Reasonable alternatives for high resolution work in airborne astronomy

are folded light path instruments such as Fabry-Perots or interferometric instruments whose light path may also be folded and whose resolution achieving drive stage may be kept at ambient temperatures.

Much of the data presented in this thesis were taken with a Fourier transform spectrometer. The actual description of the apparatus awaits Section 2.3, but suffice it to say that the FTS system is a beam-splitting device which acts like a lamellar grating spectrometer with just two lamellae.

This system has several advantages over a comparable FP system plus some disadvantages. The most telling point for such a comparison is the source of system noise. Under electronic, or detector noise limited conditions, a FTS has a clear advantage over a FP system of the same resolving power. This is because the FTS samples many resolution elements at once, resulting in the "Fellgett", or multiplexing advantage, first pointed out by Fellgett (1951). Individual resolution elements are encoded in a Fourier series which is recovered using FT techniques. The result (see Section 2.3.2, below) is a gain of  $\sqrt{m/8}$  in the final signal/noise ratio over a similar monochromator making the same measurements, where  $m$  = number of measurements (resolution elements). Typically we make 32 or 64 measurements, resulting in a multiplexing advantage of 2 or  $2\sqrt{2}$  if the system is electronic-detector noise limited.

We must stress, however, that the Fellgett advantage does not hold under background limited conditions. In fact, at the inception of our FTS in present use, our grating spectrometer was clearly not background limited but rather electronic noise limited. Consequently, in the early spectra obtained with our interferometer the multiplexing advantage

resulted in FT spectra whose sensitivity was two times that which the zero path (no interference) signal-to-noise ratios would indicate. Since then, with improvements in detector design and processing, filtering and electronics we have seen our sensitivity improve by over a factor of six. The Fellgett advantage is now not so evident and it is likely that we are approaching background limited performance.

It should be noted that if the background limit is due to changes in emissivity, transmission or turbulence along the light path, it should be possible to regain much of the Fellgett advantage through use of a reference detector which monitors these changes. If, however, photon noise dominates, no such deconvolution is possible and the Fellgett advantage vanishes.

It is also true that the Fellgett advantage is only useful if one wishes to sample all of the  $m$  points in the FT spectrum. In the presence of a continuum one many typically wish to sample eight continuum points in addition to the spectral line of interest. Thus, our sampling of 32 or 34 points corresponding to 16 or 32 resolution elements requires that there be two or four spectral lines of interest in the bandpass of our instrument. In the FIR this is not an unusual situation, the case where there are not two or more interesting lines in our grating bandpass of  $2.2 \mu\text{m}$  is the exception rather than the rule (see the Appendix).

In the absence of the Fellgett advantage, the FTS system has several other features which make it a desirable system.

- 1) The interferometer is a ready extension of our grating spectrometer which acts as an order sorter for the interferometer. We presently

use our order sorter with 4x4 mm entrance slits which results in a resolution  $R \sim 200$ .

2) The FTS has advantages of a grating instrument that a FP system doesn't have. Our FTS system is fully as tunable as our grating spectrometer, 100-200  $\mu\text{m}$  continuous coverage in first order of our grating. FP systems often do not supply full tunability, requiring preflight selection of which order sorting fixed FP plates will be used. This may limit the instrument to about four spectral regions of interest during a flight. A third characteristic our FTS shares with a grating instrument is the ability to illuminate multiple detectors. Our grating spectrometer at present contains two detectors working in adjacent wavelength regimes. This is a great boon for "search" capabilities, i.e., if the rest frequency of the species in question is unknown, or if we wish to sample lines which are closely spaced in the FIR spectrum.

3) An advantage unique to the FTS is absolute wavelength calibration. The wavelength scale of our FT spectra are determined solely by the step and burst sizes with which a mirror is advanced (see Section 2.3 below). Thus we require no "in-flight" wavelength calibration. If the step size is known to relative accuracy  $\Delta$ , then the absolute wavelength scale of the FT spectrum must also be precise to  $\Delta$ .

4) The FTS shares an advantage with the FP instrument over a grating spectrometer in that the spectral resolution may be continuously varied without losses in system throughput. Furthermore, only minor modifications are required to increase the travel of the drive stage. Our initial drive stage had a 5 cm travel corresponding to a maximum spectral resolution of  $.1 \text{ cm}^{-1}$ . Since then, we have increased the drive

stage travel to 16 cm corresponding to a factor of 3.2 increase in spectral resolution. The design modifications were minor, and the new drive stage performed quite well on its first flight -- confirming the existence of the  $^2\Pi_{1/2}$  ( $J=3/2 \rightarrow J=1/2$ ) OH emission features in the BN-KL region of the Orion Nebula (Viscuso et al. 1985).

5) A final calling card for the FTS instrument is cost and ease of construction. The interferometer was conceived, designed and flown in a period of just seven weeks in March-April 1981. The total cost was under \$2000.

### 2.3. Interferometer.

#### 2.3.1. Theory.

Before giving a detailed description of the design and operation of the interferometer used for data in this thesis, let us first digress to give a simple description of how a Fourier encoding spectrometer works. We follow the notation of Harwit and Sloane (1979).

In the simplest of FTS systems, a collimated coherent beam is split evenly across two reflecting mirrors, one of which is movable, call it mirror M; the other, being fixed, call it mirror F. Imagine a monochromatic wavefront of frequency,  $\nu$ , and electric field amplitude A incident on this system. As mirror M moves a physical displacement,  $\epsilon$ , the optical path length of the beam from M is varied by a distance  $2\epsilon$ . Thus, the return beam from M lags the return beam from F by a phase  $\phi = 4\pi\nu\epsilon$  where  $\nu$  now is the wave number. At zero path ( $\epsilon = 0$ ), the returned amplitude from either mirror is  $A_0 = A/2$ . At path difference  $\epsilon$ , the return amplitude from M+F is given by

$$A(\epsilon) = A/2 [1 + \exp(4\pi i v \epsilon)]$$

Thus, the intensity at the detector (after the beams have been recombined) is

$$n(\epsilon) = A(\epsilon)^* A(\epsilon) = A^2/2 [1 + \cos(4\pi v \epsilon)] \quad [2.1]$$

If the incident wavefront is the superposition of many wavenumbers,  $v$ , each with its own intensity, then the total intensity in the frequency interval  $v \rightarrow v+dv$  may be written  $\psi(v)dv$  so that

$$\begin{aligned} n(\epsilon) &= 1/2 \int_0^{\infty} \psi(v) [1 + \cos(4\pi v \epsilon)] dv \\ &= 1/2 \psi_0 + 1/2 \int_0^{\infty} \psi(v) \cos(4\pi v \epsilon) dv \end{aligned} \quad [2.2]$$

where  $\psi_0 \equiv \int_0^{\infty} \psi(v) dv$  is the intensity at zero path. The interferogram thus consists of a modulated part (the integral) superposed on a fixed D.C. offset. The physically interesting part is the integral:

$$n'(\epsilon) \equiv 1/2 \int_0^{\infty} \psi(v) \cos(4\pi v \epsilon) dv$$

Since  $\psi(v)$  and cosine are symmetric functions, we may write:

$$n'(\epsilon) = 1/4 \int_{-\infty}^{\infty} \psi(v) e^{4\pi i v \epsilon} dv$$

where we have replaced  $\cos(4\pi v \epsilon)$  by  $e^{4\pi i v \epsilon}$  as the anti-symmetric sine term will vanish. Thus defining  $x \equiv 4\pi v$  we have:

$$n'(\epsilon) = 1/16\pi \int_{-\infty}^{\infty} \psi(x/4\pi) e^{ix\epsilon} dx$$

We recognize the integral as the Fourier transform of  $\psi(v) \equiv \Psi(4\pi v)$ , thus:

$$\eta'(\epsilon) = 4\pi/16\pi \Psi(4\pi\epsilon) \text{ or,}$$

$$\Psi(4\pi\epsilon) = 4\eta'(\epsilon)$$

Thus the signal at the detector,  $\eta'(\epsilon)$ , is proportional to the Fourier transform of the incident waveform  $\psi(v)$

$$\begin{aligned} 1/4\pi \int_{-\infty}^{\infty} \Psi(4\pi\epsilon) e^{-4\pi i\epsilon v} 4\pi d\epsilon \\ = 4 \int_{-\infty}^{\infty} \eta'(\epsilon) e^{-4\pi i\epsilon v} d\epsilon \\ + 2\pi\psi(v) = 16\pi \int_{-\infty}^{\infty} \eta'(\epsilon) e^{-4\pi i\epsilon v} d\epsilon \end{aligned}$$

or again appealing to symmetry:

$$\psi(v) = 16 \int_0^{\infty} \eta'(\epsilon) \cos(4\pi\epsilon v) d\epsilon$$

To precisely recover  $\psi(v)$ , we must sample  $\eta(\epsilon)$  continuously from zero-path to infinity and perform the cosine transform of  $\eta'(\epsilon)$ . In practice, of course, it is impossible to sample the entire interferogram. Instead, we sample  $\eta(\epsilon)$  at  $n$  discrete, evenly spaced points a distance  $\Delta$  apart along our total travel of  $(n-1)\Delta$ . The step size,  $\Delta$ , is chosen such that  $\Delta = 1/[4(v_{\max} - v_{\min})]$ , where  $v_{\max}$  is the maximum frequency to be sampled and  $v_{\min}$  is the minimum sampled frequency (see Section 2.3.3 for comments on choosing step size and its relation to the

Nyquist sampling rate). From this point on, we drop the superscript from  $n'(e)$ .

The interferogram thus sampled may be discretely transformed to form an estimate  $\hat{\psi}_1(\nu)$  of the true spectrum  $\psi(\nu)$ ,

$$\hat{\psi}_1(\nu) = 16 \sum_{r=0}^{n-1} n(r\Delta) \Delta \cos(4\pi r\Delta\nu)$$

We wish to evaluate  $\hat{\psi}(\nu)$  at the  $n$  discrete frequencies  $\nu_s$  given by  $\nu_s = \nu_{\min} + s\delta$  for  $s = 0, 1, \dots, n-1$  and  $\delta \equiv (\nu_{\max} - \nu_{\min}) / (n-1)$ .

The true estimator of  $\psi(\nu)$  in the frequency range  $\nu_{\min} \leq \nu_s \leq \nu_{\max}$  is given by:

$$\hat{\psi}(\nu) = \hat{\psi}_1(\nu)\delta = \hat{\psi}_1(\nu)/4(n-1)\Delta \text{ or,}$$

$$\hat{\psi}(\nu) = 4/(n-1) \sum_{r=0}^{n-1} n(r\Delta) \cos(4\pi r\Delta\nu) \quad [2.3]$$

We formally rewrite this as the matrix equation:

$$\hat{\Psi} = A \eta$$

where  $\hat{\Psi}$  and  $\eta$  are the column vectors defined by:

$$\hat{\Psi} = \begin{bmatrix} \hat{\Psi}(v_{\min}) \\ \hat{\Psi}(v_{\min} + \delta) \\ \vdots \\ \hat{\Psi}(v_{\max}) \end{bmatrix} \quad \eta = \begin{bmatrix} \eta(0) \\ \eta(\Delta) \\ \vdots \\ \eta[(n-1)\Delta] \end{bmatrix}$$

and  $A$  is an  $n \times n$  matrix whose elements  $a_{sr}$  are defined by

$$a_{sr} = 4/(n-1) \cos[4\pi r\Delta(v_{\min} + s\delta)]$$

for  $s, r = 0, 1, \dots, n-1$ .

### 2.3.2. The Fellgett Advantage.

The factor of  $4/(n-1)$  in equation 2.3 above is very important. This is the term which leads to the Fellgett advantage.

The Fellgett advantage is realized if the following criteria apply:

- 1) The dominant source of noise is detector-electronic noise, i.e., the noise is independent of photon flux.

- 2) The noise of each measurement,  $e_j$ , has zero mean;  $\langle e_j \rangle = 0$  (where  $\langle \rangle$  indicates a time average expectation value).
- 3) The noise between various measurements  $n(e_i), n(e_j)$  is uncorrelated, i.e.,  $\langle e_i e_j \rangle = 0$ .
- 4) The noise has a variance defined by  $\langle (e_j)^2 \rangle = \sigma^2$ .

Under these circumstances, the expectation value of the estimator  $\hat{\Psi}$  is given by:

$$\langle \hat{\Psi} \rangle = \psi(v)$$

and we may write:

$$\hat{\Psi} - \psi = A e + \hat{\Psi}_j - \psi_j = a_{s,0} e_0 + \dots + a_{s,n-1} e_{n-1}$$

where  $e$  is the noise column vector.

We define by  $\epsilon_{v_s}$  the variance of the spectral estimator for frequency  $v_s$ ,  $\hat{\Psi}(v_s)$

$$\epsilon_{v_s} \equiv \langle [\hat{\Psi}(v_s) - \psi(v_s)]^2 \rangle = \sigma^2 (a_{s,0}^2 + \dots + a_{s,n-1}^2)$$

the average mean square error,  $\epsilon$ , is given by:

$$\begin{aligned} \epsilon &\equiv (1/n) \sum \epsilon_{v_s} = \sigma^2/n (a_{0,0}^2 + a_{1,1}^2 + a_{n-1,n-1}^2) \\ &= \sigma^2/n \text{Trace} (A \cdot A^T) \end{aligned}$$

$$= 16\sigma^2/[n(n-1)^2] \sum_{r=0}^{n-1} \sum_{s=0}^{n-1} \cos^2[4\pi r\Delta(v_{\min} + s\delta)]$$

$$= 8n\sigma^2/(n-1)^2 + 8\sigma^2/[n(n-1)^2] \sum_r \sum_s \cos[8\pi r\Delta(v_{\min} + s\delta)]$$

$\sim 8\sigma^2/n$  for large  $n$ .

Thus, if we measure a variance  $\sigma^2$  for each  $n(\epsilon)$ , then we will measure a variance in the transform spectrum which is smaller by a factor of  $(8/n)^{1/2}$ . This Fellgett advantage is quite powerful when a detection system is detector-electronic noise limited. For a discussion of the relative merits of multiplexing instruments, see Harwit and Sloane (1979).

Prior to the introduction of J-FETs and better detector processing techniques, our FTS system was clearly detector-electronic noise limited. Figure 2.1 shows the Fourier transform spectrum representing the first astronomical detection of the  $J = 16 \rightarrow 15$  rotational transition of highly excited CO (Stacey et al. 1983). This spectrum is the average of three spectra taken in January 1982, while observing the BN-KL region of the Orion nebula. For each spectrum, we sampled the interferogram 33 times and integrated 10 seconds at each point. Thus, we expect to see a factor of two ( $= (n/8)^{1/2}$ ) increase in sensitivity in the Fourier transform domain relative to raw data. At zero path we measure a system NEP,<sup>1</sup> including all losses, of  $\sim 3.6 \times 10^{-13} \text{ W Hz}^{-1/2}$ . The grating bandpass is roughly Gaussian in shape for an extended source such as BN-KL. The dashed line represents a least squares Gaussian fit to the data, ignoring the telluric water vapor absorption features at 161.90  $\mu\text{m}$

<sup>1</sup> Noise Equivalent Power (NEP) is the power incident on the telescope which produces a signal/noise ratio of one, in one second of integration.

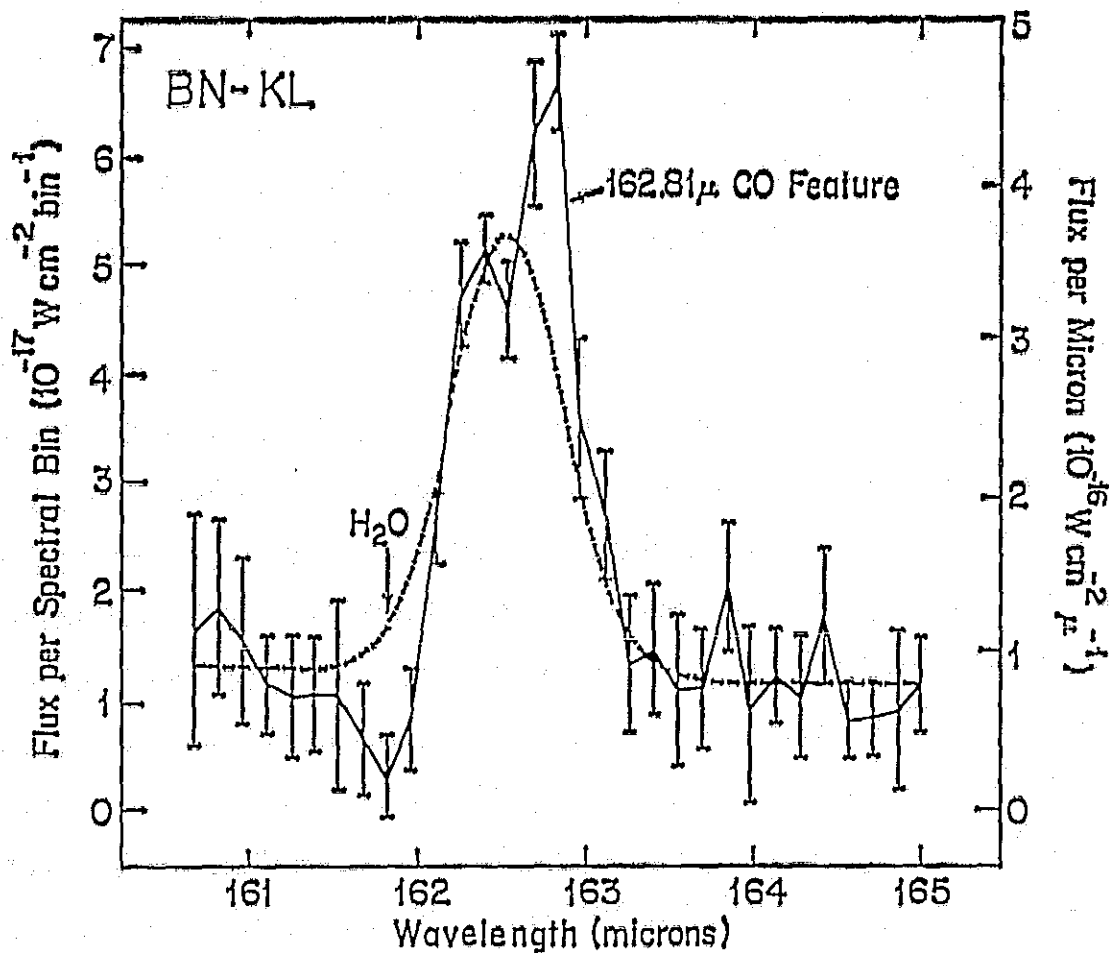


Figure 2.1 Fourier transform spectrum of the BN-KL region of the Orion Nebula showing the first astronomical measurement of the  $J = 16 \rightarrow 15$  ( $162.81 \mu\text{m}$ ) rotational transition of highly excited CO (Stacey et al. 1983). The spectrum has been fit with a least squares Gaussian centered at  $162.55 \mu\text{m}$  which accurately mimics our grating profile. The CO feature and nearby  $\text{H}_2\text{O}$  features at  $161.90 \mu\text{m}$  and  $163.53 \mu\text{m}$  have been ignored in the fitting process.

and 163.53  $\mu\text{m}$ , and the 162.81  $\mu\text{m}$  CO feature. If one measures the deviations of the data from this best fit, one calculates a system NEP  $\sim 1.9 \times 10^{-13} \text{ W Hz}^{-1/2}$  -- a factor of two better than the NEP of the interferogram -- as predicted.

Recent advances in electronics and detector processing have increased our sensitivity so that our interferometer - spectrometer system is now typically characterized by system NEP's  $\sim 5 \times 10^{-14} \text{ W Hz}^{-1/2}$  at zero path. Recent spectra show that the Fellgett advantage is much smaller than predicted -- resulting in less than 20% improvement in the Fourier transform domain. We take this as good indication that our system is no longer detector-electronic noise dominated and approaches the sensitivity limit imposed by random background fluctuations.

### 2.3.3. Choosing Burst Size: The Nyquist Rate.

If we wish to sample all the frequencies,  $\nu$ , of  $\phi(\nu)$  from the  $\nu = 0$ , D.C. term to some maximum frequency,  $\nu_{\text{max}}$ , we must sample  $\eta(\epsilon)$  at the so-called Nyquist rate to avoid aliasing.<sup>2</sup> The Nyquist, or sampling theorem (see, for example, Papoulis 1977), simply states that to obtain an unaliased spectrum in the frequency domain, we must sample the interferogram at a rate equal to twice the highest unaliased frequency.

---

<sup>2</sup> Aliasing refers to uncertainty concerning the spectral order of the interferogram, or transfer from one order to another.

For the interferogram, this means we must sample  $n(\epsilon)$  every  $1/4\nu_{\max}$  cm. (Remember, every physical displacement  $\epsilon$  corresponds to an optical path length increment  $2\epsilon$ .) For a drive stage 5 cm long at a frequency  $\nu_{\max} \sim 67 \text{ cm}^{-1}$  (150  $\mu\text{m}$ ) this means we must sample  $n(\epsilon)$  over 1000 times for just one spectrum. Clearly this would be prohibitive in terms of both integration time and the computer time needed to perform a 1000 point Fourier transform. To both circumvent this problem, and especially to reduce the background flux incident on the detectors, we employ our high resolution spectrometer (see Section 2.4, below) to act as an order sorter and greatly reduce the number of frequencies to be sampled. At 150  $\mu\text{m}$ , our two-detector spectrometer samples a total bandpass of roughly 2  $\mu\text{m}$  corresponding to  $\Delta\nu_{\text{spect}} \sim .9 \text{ cm}^{-1}$ . Thus we need only sample fast enough such that we sample all frequencies between  $\nu_{\min}$  and  $\nu_{\max}$  where  $\nu_{\min}$  is determined by  $\nu_{\min} \leq \Delta\nu_{\text{spect}} \leq \nu_{\max}$ . This may be ensured by choosing the burst size,  $\Delta$  such that  $\Delta = 1/[4(\nu_{\max} - \nu_{\min})]$ .

In practice, we choose  $\Delta$  by the following convention. First, choose the central wavelength,  $\nu_c$ , of the Fourier spectrum. Typically this wavelength is chosen such that it falls halfway between the peak spectral response of the two channels in the spectrometer. The central wavelength is determined by  $\nu_c = (m+1/2)/4\Delta$ , where  $m$  = interferometer order, usually  $\sim 30$ -40 for our 5 cm travel stage. Intuitively,  $m$  denotes the number of interfering wavefronts skipped with every burst. The infrared frequency  $\nu_c$  is aliased through this technique to a much lower frequency  $\nu'_c = \nu_c/m$ . The factor of  $1/2$  above, then, ensures we sample each aliased frequency twice per wavefront. Now  $\Delta$  is

physically constrained by the drive stage travel such that if we choose to use  $n$  bursts to sample our spectrum, we must have  $n\Delta \leq 5$  cm. Typically  $n = 32$ , so that  $\Delta \sim 1500$   $\mu\text{m}$ . The free spectral range of the resultant spectrum is given by the difference between adjacent interferometric orders or,  $\Delta\nu_{\text{FSR}} = \nu_c^2 [4\Delta(1/m - 1/(m+1))]$ . Having chosen the step size,  $\Delta$ , one may assign frequencies to the Fourier transform spectrum using the reverse of the above transformations.

#### 2.3.4. Functional Description.

Our interferometer was first described in a paper by Harwit et al. (1981). The interferometer acts like an all-reflecting lamellar grating spectrometer with just two lamellae (see Figure 2.2). The infrared radiation from the KAO's f/17 beam is reflected off a dichroic and brought to a focus at plane mirror A. The visible light passes through the dichroic and is imaged within the offset guider reticles. (Designed by Prof. James R. Houck.) At mirror A is a 4 mm wide entrance slit which ensures our sampling within the primary diffraction lobe of the telescope ( $\sim 6$  mm from 1<sup>st</sup> null to 1<sup>st</sup> null at 150  $\mu\text{m}$ ) and thus sampling a coherent beam. Mirror A diverts the diverging beam to plane mirror B which reflects the light into C. C is a 45 cm focal length off-axis paraboloid which collimates the f/17 beam into a beam  $\sim 2.5$  cm in diameter. The collimated beam then strikes plane mirror D which is aligned so that the circular beam is split evenly across mirrors E and F. Mirror E is the plane mirror whose movement relative to plane mirror F causes the interference. These mirrors have been aligned so

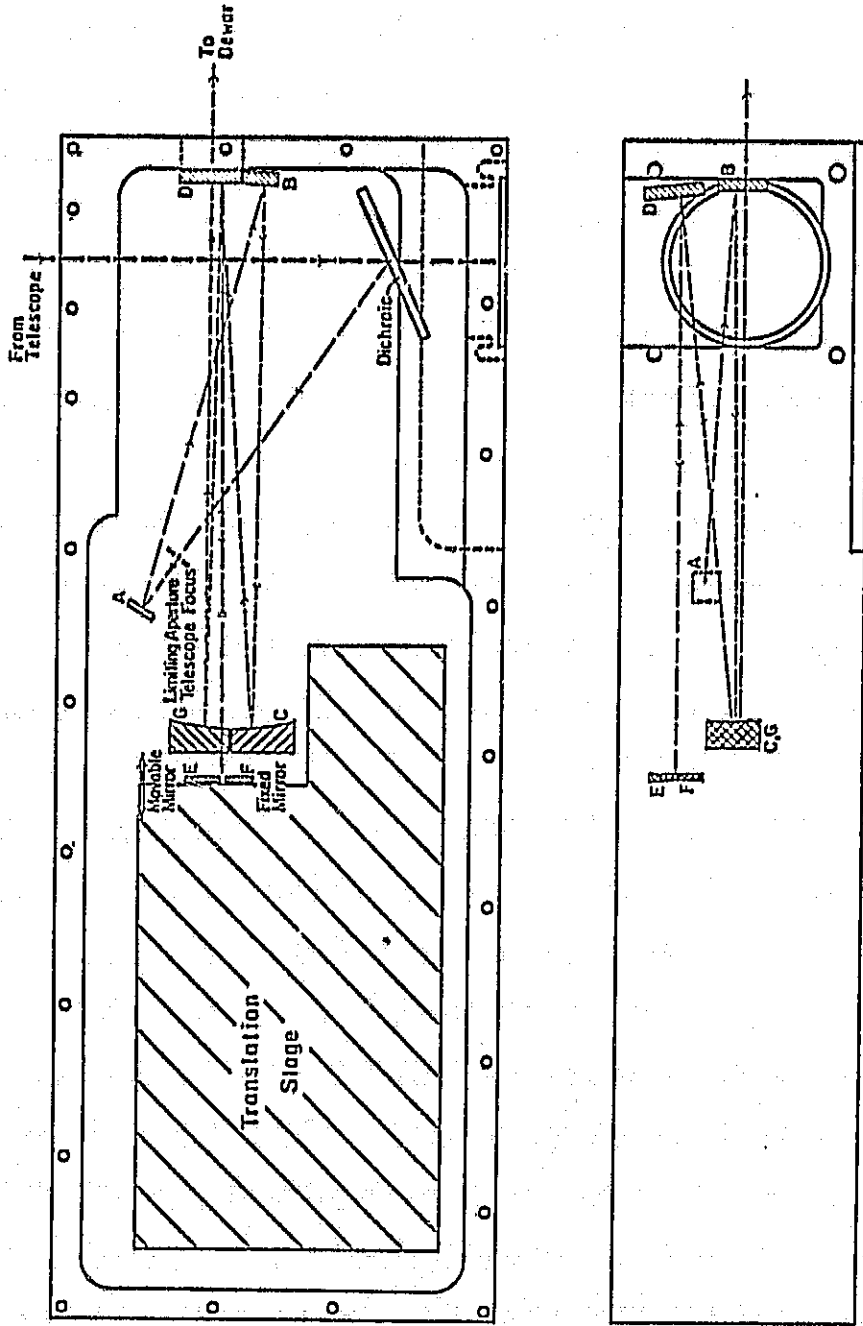


Figure 2.2. Our lamellar grating interferometer top view (top) and side view (bottom). The dashed line shows the light path through the system.

that at zero path there is just a fraction of a millimeter between the two, thus minimizing the effects due to diffraction. As E moves, the path length,  $2\epsilon$ , of the return beam is varied. Figure 2.2 shows that the path of the collimated beam is parallel to the direction of movement of the drive stage and above mirrors C and G. Thus, there is no blockage of the light from F as E moves to full path difference. The beams from mirrors E and F are recombined at D before striking G, a second 45 cm focal length paraboloid which refocuses the beam to  $f/17$  and images it on the entrance slit of the spectrometer.

Note that when mirrors E and F are coplanar, the spectrometer receives exactly (minus losses due to the seven reflections ~ 30%) the same radiation it would receive from the telescope in the absence of the interferometer.

A 5 cm travel drive stage was used for all of the interferometer data presented in this thesis. The drive stage is commercially available (Aerotech, Inc., Allison Park, PA 15101) with an accuracy better than 1 part in  $10^3$  and with somewhat better reproducibility. The stage is driven by a stepper motor and geared in such a way that one step of the stepper motor corresponds to a 2  $\mu\text{m}$  translation of the drive stage. We were able to accurately calibrate the step size through our detections of the  $J = 17 \rightarrow 16$  and  $J = 16 \rightarrow 15$  rotational transitions of highly excited CO found in the BN-KL region of the Orion nebulae. The wavelengths of these transitions are known to very high accuracy (Todd et al. 1976). These detections determined that our step size was actually 1.998  $\mu\text{m}$  -- within the advertised accuracy of the drive stage.

The spectral resolution of our drive stage is determined by the longest optical path length difference introduced into our interferogram. For a 5 cm travel, the optical path difference is 10 cm corresponding to a spectral resolution of  $.1 \text{ cm}^{-1}$ . At  $157 \mu\text{m}$ , this corresponds to a resolution  $R \equiv \lambda/\Delta\lambda \sim 650$ .

This resolution estimate is based on the standard Rayleigh criterion. That is, we will resolve two lines of equal intensity as independent spectral elements if they are separated by  $\Delta\nu \sim .1 \text{ cm}^{-1}$ . The full width half maximum (FWHM) of any unresolved spectral line may be made a factor of two narrower than this through proper choice of burst size. We define our spectral definition,  $D$ , as  $D \equiv \lambda/\Delta\lambda_{\text{FWHM}} = 2R$ . Thus, we may measure line widths and wavelengths a factor of two better than the resolution. The definition of our 5 cm travel stage is  $D \sim 1300$ , or  $\Delta v = 230 \text{ km/sec}$ .

To fully achieve this resolution, one must sample the interferogram at both positive and negative path lengths. However, if one a priori knows that the interferogram has begun with a sample at zero path, then one may mathematically reflect the data about zero path, as we are assured by symmetry that signals measured at a positive path difference,  $\epsilon$ , must be the same (within the noise) as those measured at negative path difference,  $-\epsilon$ . In practice, determination of zero path has been a straightforward process. One first eyeballs the movable mirror,  $E$ , to within a fraction of a millimeter of zero path on the negative side. Then, with the grating spectrometer set at a suitable wavelength, typically  $118 \mu\text{m}$ , one single steps the movable mirror through zero path producing a sinusoidal fringe pattern. If one then repeats the process

at two additional widely separated wavelengths, say 140  $\mu\text{m}$  and 163  $\mu\text{m}$ , avoiding rational relations between wavelengths, one may then unambiguously determine which fringe peak is common to all wavelengths. This fringe peak must then be zero path and zero mirror-position is then redefined as a convenient number, usually as step 1000, and used as the reference point throughout the flight.

### 2.3.5. Design Limitations.

The efficiency of our interferometer is strictly governed by the modulation depth, i.e., the fringe visibility near zero path. As can be seen from equation 2.2, for a sufficiently narrow bandpass, as one steps the movable mirror about zero path, the two beams will interfere to form a sinusoidally varying interferogram of maximum power  $P = \psi_0$  and minimum power  $\emptyset$ . This is the ideal system; let us denote its efficiency by  $\epsilon = 1$ . In reality, various diffraction effects lower the coherence of the recombining beams. This results in both a lowering of the peak interference signal,  $P$ , and an increase in the valley signal,  $V$ . The efficiency,  $\epsilon$ , may then be defined as  $\epsilon \equiv (P-V)/P$ . We can see that if there is no modulation, i.e., no interference of beams,  $P = V$  and  $\epsilon = \emptyset$ . For coherent lab sources, we have obtained fringe visibility ratios  $P:V$  as high as 6:1 resulting in an 83% efficient interferogram. Typical in-flight fringe visibility is ~ 4:1 resulting in a 75% efficient scan. It has been found that the fringe visibility is extremely sensitive to the gap between mirrors E and F at zero path. Fringe visibilities as high as 6:1 with a gap of .1 mm are degraded to ~ 2:1 if the gap is allowed to grow as large as .5 mm.

An unfortunate consequence of the original design for the interferometer is that mirror E had to be aligned such that its reflecting surface was not perpendicular to its direction of travel. Thus, the collimated beam walks across mirror G as E travels and consequently also moves across the secondary of the spectrometer. Portions of the beam eventually walk off the secondary resulting in a loss of light from E at long path lengths, hence a loss of both modulation depth and absolute signal level. An interferogram of a strong continuum source (BN-KL in Orion) then has the characteristic "droopy shoulder" appearance of Figure 2.3a. The Fourier transform of such an interferogram invariably shows a huge first cosine term. The data may be mathematically corrected by fitting a least squares line to the interferogram and removing this baseline from the data (Figure 2.3b). Recently, this problem has been alleviated entirely through introduction of corner mirrors. The return beams from corner mirrors E and F are then both parallel to the direction of travel of E resulting in the elimination of walk-off problems.

## 2.4. Spectrometer.

### 2.4.1. Layout and Functional Description.

The spectrometer used for the observations presented in this thesis is a fully liquid helium cooled grating spectrometer operated in a Littrow mode. Essentially, it is an improved version of the spectrometer originally described by Houck and Ward (1979) and later improved

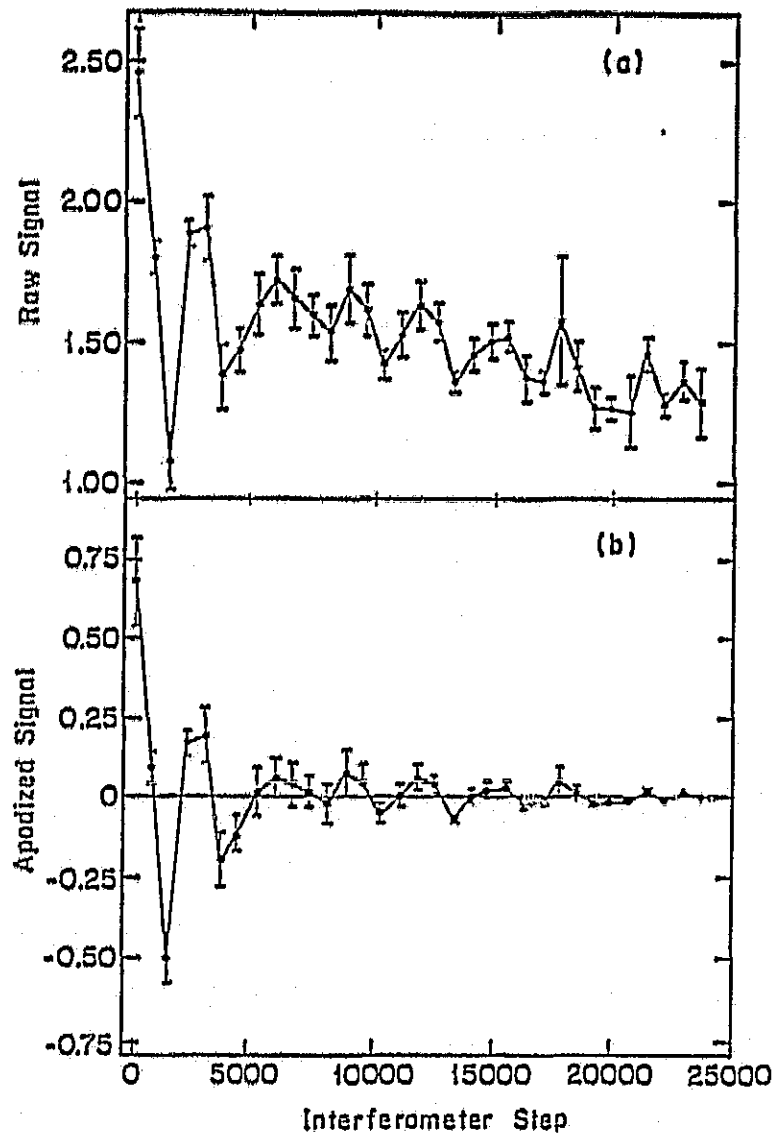


Figure 2.3 a&b. Apodization of an interferogram. Figure 2.3a shows the average of four interferograms taken of the BN-KL region of the Orion Nebula of September 23, 1981. Zero path is the high point on the left and the point 33 on the far right is data taken at largest travel (5cm) of our drive stage. Error bars are one standard deviation from the mean. Figure 2.3b shows the same interferogram following droopy shoulder removal and apodization with a triangle (Bartlett) window. The D.C. offset has been subtracted out.

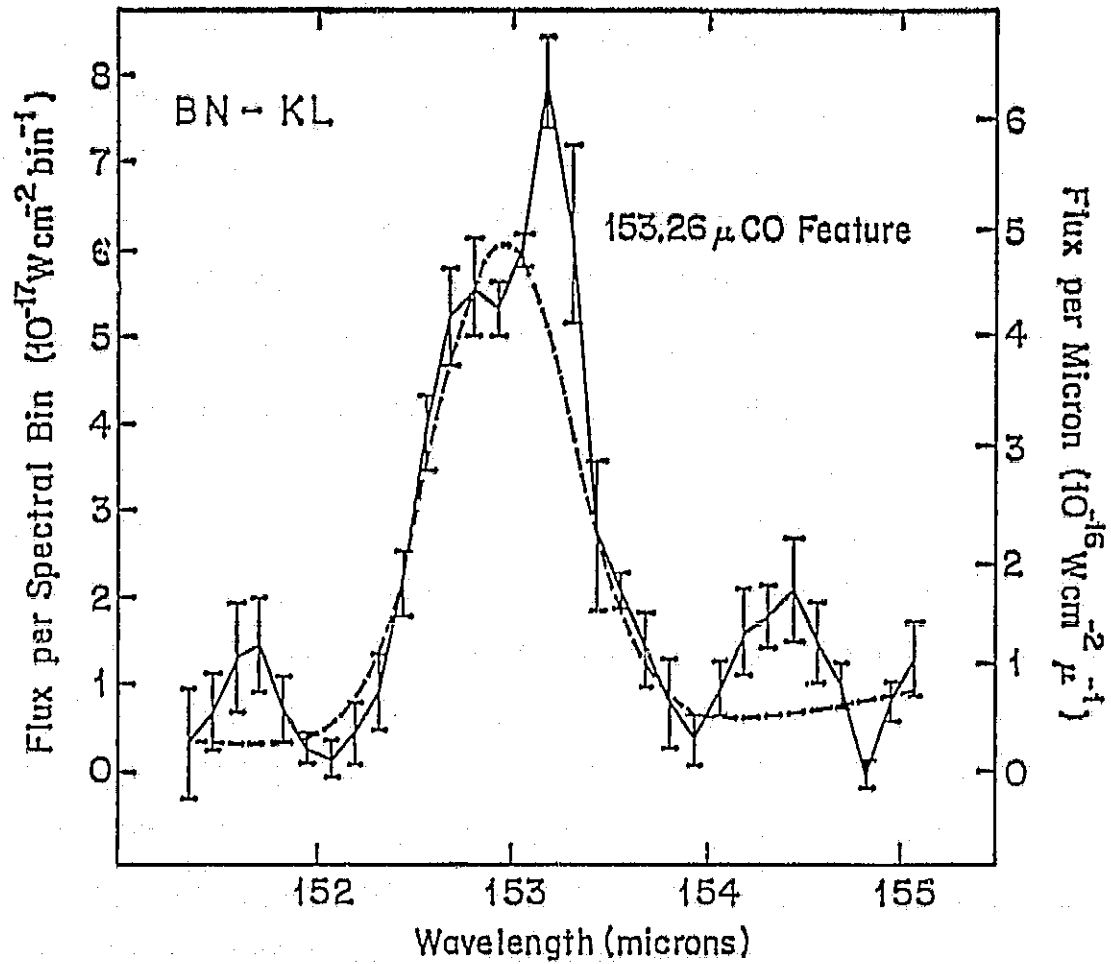


Figure 2.4. Fourier transform spectrum of the BN-KL region of Orion. This spectrum is the Fourier transform of Figure 2.3b, following reflection about zero path. The fitted Gaussian represents the grating instrumental profile. The feature at 153.3  $\mu\text{m}$  is the first astronomical detection of the  $J = 17 \rightarrow 16$  rotational transition of shocked  $^{12}\text{CO}$  (Stacey et al. 1982).

and reconfigured for the f/17 beam of the KAO by Melnick (1981). As can be seen in Figure 2.5 the collimator is a Cassegrain system. Light entering the spectrometer at A passes through the far infrared filter at B before being deflected to the secondary by a 45° plane mirror at C. Just in front of C is the entrance slit. C is set slightly off-axis so that the return diffracted beam misses the mirror. The secondary illuminates the 3" primary, D, which then sends the collimated beam to the diffraction grating at E. The diffracted beam then is de-collimated and exits the collimator at F. The collimator bolts directly onto the  $\lambda$ He-cooled work surface, which is the bottom of the  $\lambda$ He can. The beam at F is deflected by two 45° mirrors displaced ~ 4 mm along the direction of dispersion on the work surface. These mirrors send the beam onto the exit slits located at the entrance to the light cones of the two detectors. All of the structural parts of the collimator are constructed of stress-relieved aluminum.

#### 2.4.2. Optics.

The effective focal ratio of the collimator may be adjusted from f/6.5 (to match the Lear telescope) to f/17 (to match the KAO telescope) by changing optics. The f/6.5 optics were made of low thermal expansion Pyrex glass by 3-B Optical Co. (Gibsonia, PA). Both the concave primary (radius of curvature,  $R_C = 38.9$  cm) and the convex secondary ( $R_C = 24.15$  cm) have spherical figures as the diffraction lobe of both the Lear and KAO telescopes is large enough at 150  $\mu$ m to make spherical aberration negligible. Glass mirrors have two inherent problems. They

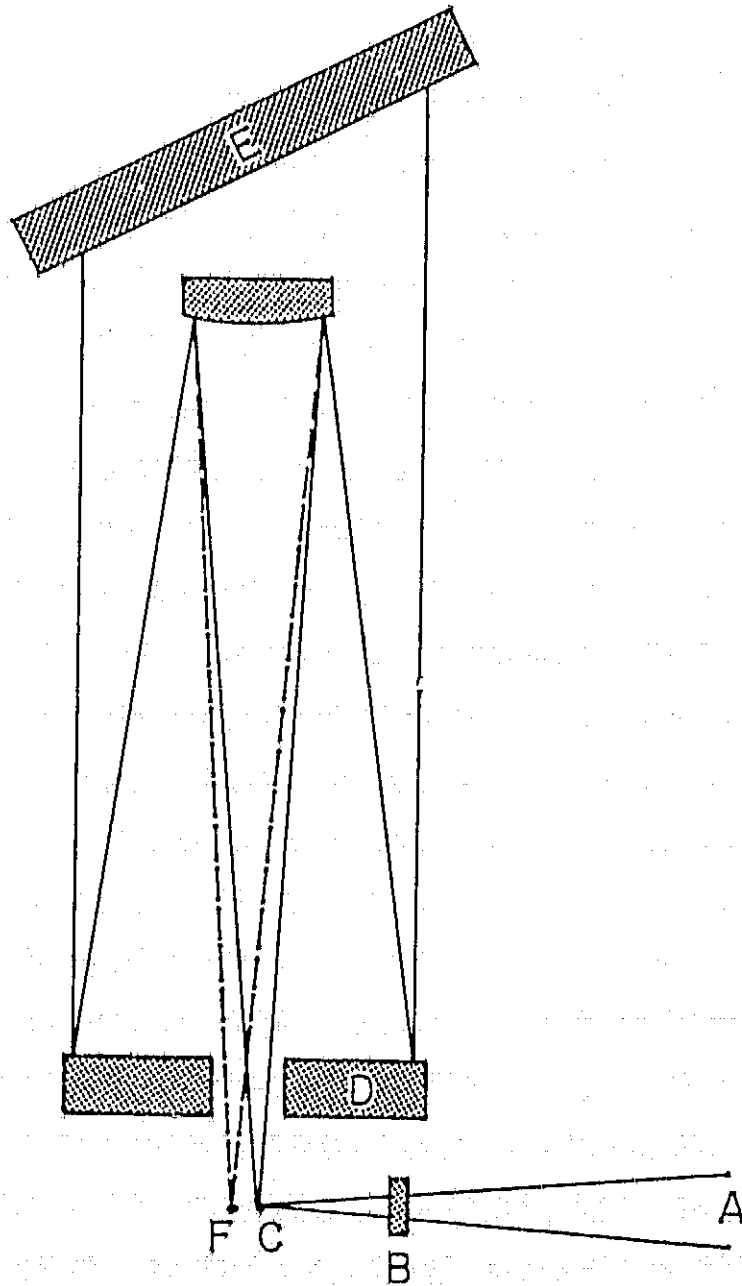


Figure 2.5. Schematic layout of liquid helium cooled grating spectrometer. (After Melnick 1981)

have a large thermal mass and time constant and shrink differentially relative to the aluminum collimator walls. Thus, the focal length of the instrument must be adjusted at room temperature so that the focus of the instrument shifts the correct amount as the collimator cools to liquid helium temperatures. This differential contraction results in a shift in the focus ~ 8 mm. The advent of high surface quality pure aluminum mirrors has eliminated both of these problems. Our f/17 optics are all aluminum, primary  $R_c = 27.06$  cm, secondary  $R_c = 5.76$  cm, machined by a diamond tool at Aeroresearch Corporation, Great Neck, NY. Essentially all of the f/17 collimator is then aluminum, which means the unit shrinks uniformly and therefore the focus does not shift as the collimator cools. The aluminum mirrors have the further advantage that they may be directly heat-strapped to the collimator walls through copper braiding. These straps are attached with epoxy or screws.

The all-aluminum grating (Bausch and Lomb, Rochester, NY) has been blazed at  $26.75^\circ$  and ruled at 6 lines/mm for first order work at  $150 \mu\text{m}$ . The grating also has been heat-strapped to the collimator walls. A stepper motor, external to the helium dewar positions the grating. The stepper motor's motion is geared to a fiberglass rod which feeds through an O-ring in the dewar bottom. The fiberglass rod minimizes the heat load into the dewar. The grating is coupled to the motor through a set of bevel gears and a worm-wheel assembly. The stepper motor steps through 7000 steps to provide a  $30^\circ$  rotation of the grating. This corresponds to grating tunability from  $\sim 100 \mu\text{m} \leq \lambda \leq 200 \mu\text{m}$ , each step corresponding to  $\sim .019 \mu\text{m}$  at  $150 \mu\text{m}$ . The two channels are separated in wavelength space by one resolution element or  $\sim .7 \mu\text{m}$  in the f/17 configuration.

Wavelength calibration of the grating spectrometer is achieved through matching observed water vapor features in the spectra of laboratory continuum sources with the known wavelengths of these features (Traub and Stier 1976). Our stressed Ge:Ga detectors are sensitive from  $100 \mu\text{m} \lesssim \lambda \lesssim 195 \mu\text{m}$  and we generally identify a dozen or so water vapor features within this regime with which we calibrate wavelength as a function of grating step. Theoretically one should use the grating equation to make the calibrations which, for Littrow systems reads:

$$m\lambda/d = 2 \sin(\beta)$$

where  $m$  = order,  $d$  = groove spacing, and  $\beta$  = tilting angle of the grating with respect to the normal. Converting tilt angle to grating step is somewhat tedious, and it is found that in practice, a simple linear interpolation procedure between water vapor features is sufficient. The accuracy of our grating calibrations, as verified with the interferometer, is typically better than  $.2 \mu\text{m}$  or  $1/4$  resolution element.

For Lear data, these grating calibrations, as verified by in-flight spectra of calibrators, are used for the actual wavelength calibrations of the final spectrum (see section 2.6.1 below). As the interferometer is self-calibrating (see section 2.3.3), we generally take interferograms of laboratory continuum sources before take off on KAO flights to verify our grating calibrations and make any necessary adjustments. We thus ensure that the grating bandpass is centered on the expected line position and well within the free spectral range of the interferometer.

As long as the stepper motor coils are energized, the spectrometer is reproducible from scan to scan, to within a step. Between flights, the grating is re-zeroed (set to the short wavelength mechanical stop) by hand, a process which introduces a flight to flight reproducibility error of a few steps, or  $\sim .04 \mu\text{m}$ . As the spectrometer resolution is  $\sim .7 \mu\text{m}$ , this error is negligible.

Diffraction determines the smallest logical slit size to use for astronomical observations, hence maximum spectrometer resolution. The 30 cm f/6.5 telescope aboard the Lear Jet facility is diffraction limited at  $150 \mu\text{m}$  to an Airy disk  $\sim 2.2 \text{ mm}$  in diameter (null to null). This then is the optimal slit width along the direction of dispersion. For a 2.2 mm slit, we have measured system resolutions for point sources of  $R \equiv \lambda/\Delta\lambda \sim 200$ . The 91 cm f/17 telescope aboard the KAO has a diffraction lobe  $\sim 6.2 \text{ mm}$  in diameter. In flight, we generally have used a 4 mm wide slit, which results in a small ( $\sim 7\%$ ) loss in luminosity. The spectrometer in this configuration also shows a resolution of about 200.

#### 2.4.3. Dewar.

The spectrometer and helium can are contained within a 6" diameter cylindrical dewar. The helium cooled spectrometer and helium can are shielded from external radiation with an internal heat shield which fits neatly over the spectrometer helium can assembly and is attached to the top of the helium can. The heat shield is wrapped with  $\sim 20$  layers of superinsulation (aluminized mylar) and maintains a temperature

somewhat lower than 50°K. The hold time of the 3.5 liter helium can is ~ 28 hours unpumped and ~ 20 hours when the helium coolant is pumped down to 2°K. The dewar is sidelooking and the vacuum seal is preserved through the light port by a .010" thick piece of clear polyethylene. The polyethylene is rugged and transmits over 90% of the FIR radiation.

#### 2.4.4. Filters.

As our Ge:Ga detectors are sensitive to near infrared radiation, especially ~ 2  $\mu\text{m}$  where the germanium is an intrinsic photoconductor, the collimator heat shield assembly contains a series of filters to block unwanted radiation. The visible and near infrared are quite effectively blocked by a 5 mil thick piece of black polyethylene; i.e., polyethylene which has been impregnated with carbon. Since the black polyethylene scatters as well as absorbs the short wavelength radiation (McCarthy 1967), the filter is placed on the inside of the heat shield, well away from the detectors. Virtually no light is transmitted from 2.5 - 7  $\mu\text{m}$ , where the black polyethylene slowly begins to pass, reaching a transmission of ~ 8% at ~ 50  $\mu\text{m}$ . At 150  $\mu\text{m}$ , the polyethylene transmits ~ 70%.

To block unwanted radiation longward of ~ 32  $\mu\text{m}$ , we employ two helium cooled reststrahlen filters. The term reststrahlen (residual rays) is applied to certain salt crystals which display a high degree of reflection ( $\geq 90\%$ ) at wavelengths corresponding to the ionic vibrational energy bands in the crystal lattice. In the entrance cone of the spectrometer we have a 1 mm thick piece of  $\text{BaF}_2$ , which effectively blocks

from 18 - 58  $\mu\text{m}$  (Armstrong and Low 1973). The  $\text{BaF}_2$  has been antireflection overcoated (IR Labs, Tucson, AZ) for work at 157  $\mu\text{m}$  at which wavelength it transmits ~ 90%. At the exit slits, directly in front of the detectors we have installed a second reststrahlen filter, a .5 mm thick piece of  $\text{AgCl}$ .  $\text{AgCl}$  passes ~ 80% at 157  $\mu\text{m}$  and effectively blocks  $42 \mu\text{m} \leq \lambda \leq 100 \mu\text{m}$  (Armstrong and Low 1973). An alternative far-infrared reststrahlen filter would be a combination of  $\text{CsBr}$  and  $\text{KBr}$  filters in place of the  $\text{AgCl}$  (Watson 1982). These filters block  $52 \leq \lambda \leq 130 \mu\text{m}$  and also transmit ~ 80% at 157  $\mu\text{m}$ . However, these filters are much more delicate than the  $\text{AgCl}$ . They both are highly hygroscopic and  $\text{KBr}$  is quite susceptible to the thermal shock of cooling down the spectrometer.  $\text{AgCl}$  has the distinct disadvantage of possessing a deep absorption feature near 152  $\mu\text{m}$  which the  $\text{CsBr}$  and  $\text{KBr}$  do not possess (Figure 2.6). Furthermore,  $\text{AgCl}$  filters are sensitive to UV radiation and they slowly oxidize on extended contact with the brass light cones. The former problem is alleviated through care to minimize UV exposure, while the latter is eliminated by isolating the filters from any metallic contact, with Teflon shim stock. For a description of the manufacture and implementation of reststrahlen filters, see Watson (1982).

The total transmission of our spectrometer, including losses due to imperfect reflection off the collimator mirrors (10%), grating efficiency, and filter transmission efficiency is roughly 20%.

Stray light can be a major problem in a Littrow mode spectrometer, as baffling is difficult when the entrance beam is so close to the exit beam. The "channel 1" detector is particularly susceptible to stray light reflected directly back from the secondary, as this detector is on

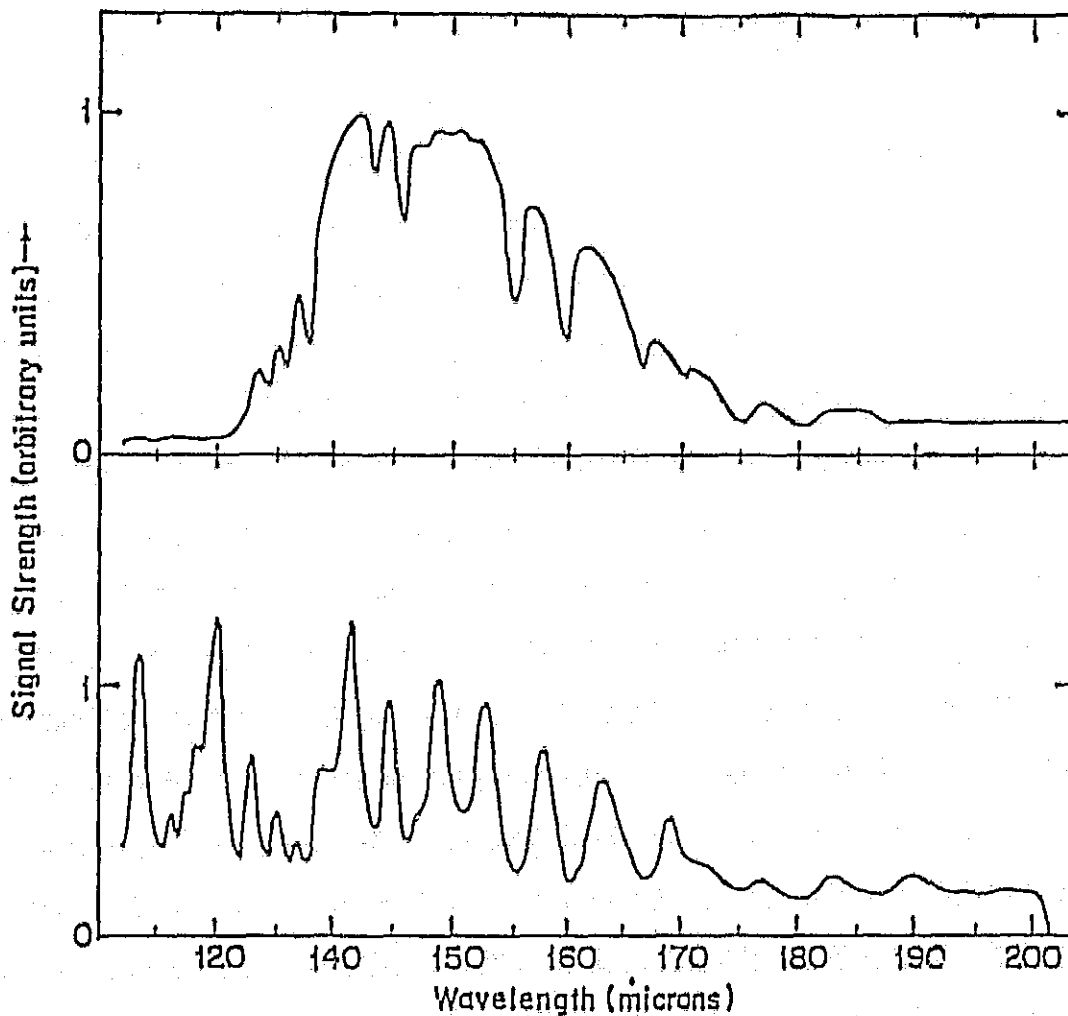


Figure 2.6. Laboratory grating calibration spectrum of liquid  $N_2$  cooled glass beads through two different sets of reststrahlen filters. Most of the absorption features in these continuum spectra are due to atmospheric water vapor absorption in the 50cm light path from the spectrometer to the glass beads. The first panel shows the spectrum obtained when CsBr and KBr are used as cut on filters to pass beyond  $\sim 135\mu\text{m}$ . The second spectrum is taken with AgCl which passes longward of  $\sim 100\mu\text{m}$ . Note the AgCl absorption feature near  $152\mu\text{m}$ . No effort has been made to deconvolve relative detector or filter response. The varying depths of  $H_2O$  features from the first to the second spectrum are due to changes in laboratory relative humidity from day to day.

the optical axis. This problem has been minimized through placing a cone of black carborundum sandpaper in the center spot of the secondary. Baffles have been placed wherever possible in the spectrometer, including an entrance baffle, a baffle at the primary and one about the secondary. The entire inside of the spectrometer has been painted black with Nextel brand black velvet spray paint mixed with carborundum. This combination reflects roughly 10% of the FIR. Residual stray light in our system is of the order 5-10%.

#### 2.4.5. Electronics.

Changes in resistance of our Ge:Ga photoconductors are converted to changes in current through a standard transimpedance amplifier (TIA) as shown in Figure 2.7. The primary advantage of a TIA is that it maintains a constant voltage drop,  $V_{Det}$ , across the detector which ensures linearity of system response. The electronics may be broken into three temperature stages: the detector resistance,  $R_D$ , and load resistance,  $R_L$ , at 2°K; the preamplifying J-FETs at 70°K; and the room temperature Operational Amplifier (OpAmp). The matched J-FETs (gain = 1) first stage of the amplifier is kept as close as possible to the detector and load resistor. This minimizes the length of the high impedance wire to the input stage, gate  $G_1$ , and hence, minimizes microphonics.

The gate  $G_2$  is kept at ground, so the action of the OpAmp is to keep the gate  $G_1$ , at ground. In operation, bias applied across the detector,  $V_B$ , acts to move free carriers through the detector resulting in a current flow,  $I_D$ . To keep  $G_1$ , at virtual ground then, the

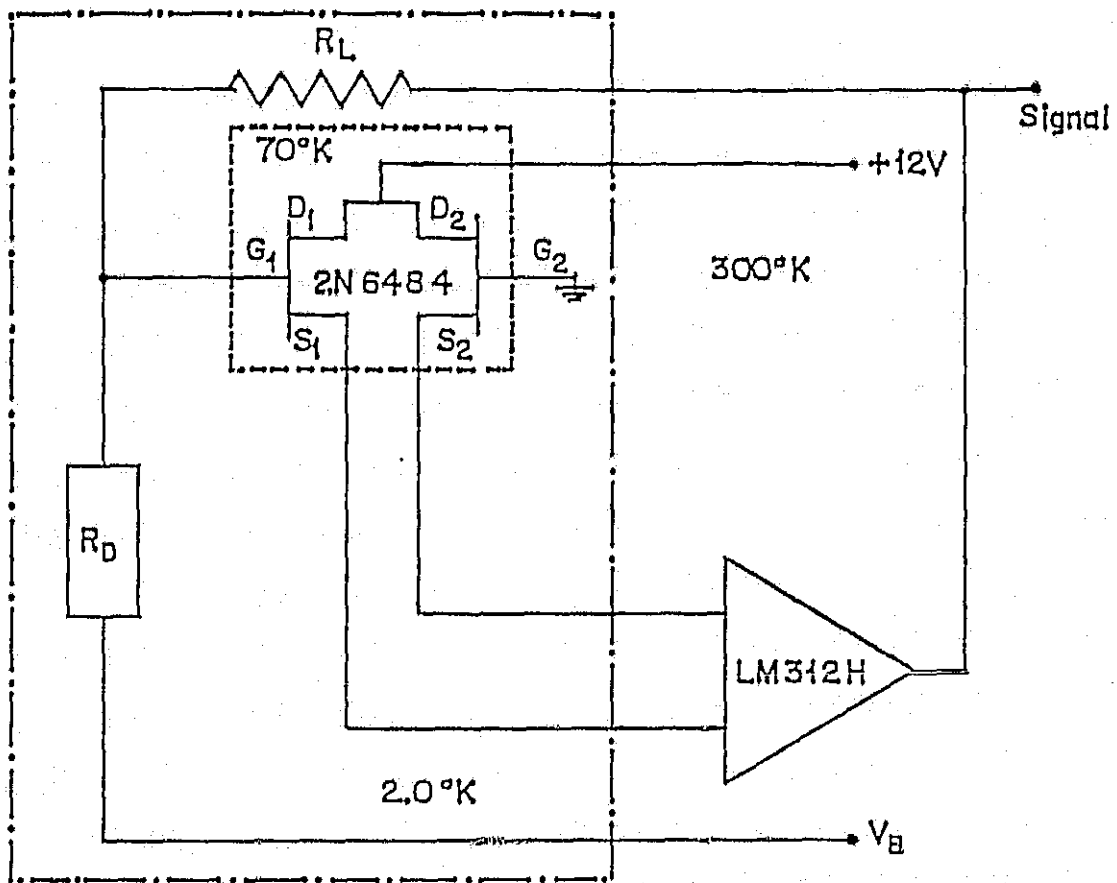


Figure 2.7. Circuit diagram for our transimpedance amplifier described in the text.

OpAmp supplies a voltage  $V_{out}$  across the load resistor such that  $V_{out} = -I_D R_L = -V_B R_L / R_D$ . The output voltage from the OpAmp is the measured signal. Changes in detector resistance thus result in changes in  $V_{out}$ . One may define a gain from the TIA as  $G = -\Delta V_{out} / \Delta V_B = -R_L / \Delta R_D$ .

Sources of noise in the TIA circuit are the Johnson noise due to the load resistor, detector-electronic noise, and microphonic pickup. Johnson noise, due to random thermal motions of electrons is given by

$$\Delta V_J = (4kTR_L \Delta f)^{1/2} \text{ volts}$$

where  $k$  = Boltzmann's constant,  $T$  = temperature ( $^{\circ}\text{K}$ ) and  $\Delta f$  is the electrical bandwidth. Taking  $T = 2^{\circ}\text{K}$ , and  $\Delta f = 1 \text{ Hz}$ , we have  $\Delta V_J = 6 \times 10^{-7} (R_L / 10^9)^{1/2}$  volts. As Johnson noise scales as  $R_L^{1/2}$  and the gain,  $G$ , (hence the signal) scales as  $R_L$ , a suitably large gain will eliminate Johnson noise. In practice, a gain of 1 is sufficient to make Johnson noise an order of magnitude smaller than background noise. Our stressed detectors have a resistance  $\sim 10^9 \Omega$  under operating background conditions, hence we use a  $10^9 \Omega$  Victoreen load resistor. At zero bias, we measure Johnson noise.

The switch-over from MOSFET preamplifiers to J-FETs and improvements in detector manufacturing techniques has effectively eliminated detector electronic noise as the primary source of noise for our system. As work space is severely limited in our dewar, and MOSFETs run at  $2^{\circ}\text{K}$  right on the work surface, the changeover to J-FETs was a slow and painful process. Paul Viscuso was instrumental in implementing this change-over. Much of the data taken for this thesis were taken with

MOSFETs which effectively limited our minimum NEP to  $\sim 2 \times 10^{-13}$  W Hz<sup>-1/2</sup>. J-FETs need to operate at temperatures above 50°K, and as our dewar has no available  $\lambda$ N<sub>2</sub> surface, the J-FET must be thermally isolated from the  $\lambda$ He surface and heated externally. At George Gull's suggestion, we stand the J-FETs off the work surface with a 1" long "L"-shaped piece of thin walled 1/4" diameter fiberglass tubing. This required some modification of the spectrometer - helium can interface. The dual J-FETs are fit into the end of the "L" section with a brass ring and heated by a 1.1 k $\Omega$  Allen-Bradley resistor. Thermal contact between the heater resistor and the J-FET is assured as the wire running between the drains of the two J-FETs is wrapped several times around the resistor and insulated in a "cocoon" of rubber cement. Care must be taken at all times not to thermally ground the J-FETs. The fiberglass tubes have been notched to minimize heat conductivity and only fine (2 mil) Formvar wire is used to make electrical contacts. The wires to the J-FETs and heaters are tied together to minimize microphonics and wound several times about the fiberglass tube to lengthen the thermal path. The wire bundle is tacked in several places along its travel with rubber cement and pulled tight to minimize microphonics. The high impedance lead between D<sub>1</sub> and the detector is the most susceptible to microphonics. Consequently, thicker wire (3 mil) is used for this lead and care is taken to minimize its length.

Whenever possible, all wires are isolated from the work surface with Kim-Wipes paper tissue and tacked with rubber cement. The Victoreen load resistor is mounted on a Kim-Wipe with rubber cement as close as possible to the detector and J-FETs. The entire system, as such, is usually insensitive to microphonic pickup.

#### 2.4.6. Stressed Detectors.

The best detectors in current use for work in the FIR are extrinsic photoconductors made by low-level doping of germanium with various impurities from columns IIIA and VA of the periodic table. Gallium doped germanium (Ge:Ga) was the material used for the first astronomical detection of a FIR fine structure line, the 88  $\mu\text{m}$  [OIII] line detected by Ward et al. in 1975.

The spectra presented in the present work were obtained with stressed Ge:Ga photoconductors. High purity germanium is doped with low levels ( $\sim 10^{14} \text{ cm}^{-3}$ ) of gallium during crystal growth. Germanium has four valence electrons and thus forms covalent bonds with four neighboring germanium atoms by sharing an electron. Gallium has three valence electrons, so at an impurity site there is a deficiency of one electron per atom in forming the crystalline bonds. The result is a hole which behaves like a positive charge loosely bound to the negatively charged gallium atom. In effect, the impurity introduces vacant discrete levels, often termed impurity acceptor levels, slightly above the valence band. Photons of sufficient energy may then excite electrons into the impurity levels leaving free holes in the top of the valence bands. In the presence of a bias field, the hole may circulate through the electronic circuit allowing current flow until the hole eventually recombines at an impurity site. The photoconductive gain,  $G_{pc}$ , is defined as the number of passes a hole makes through the detector before recombination. A second important quantity in our

photoconductor is the quantum efficiency,  $\eta$ , defined as the ratio of the number of incident photons which free a charge carrier, to the total number of incident photons. In good detector material, impurity levels are kept quite low to avoid impurity banding effects and maximize free carrier lifetimes, i.e., photoconductive gain. However, lowering the dopant concentrations effectively increases the mean free path for an impurity site ionizing photon, hence lowering the quantum efficiency. A solution is to increase the detector's physical size. For typical dopant levels the mean free path of an impurity-site ionizing photon is  $\sim 5.0$  mm, hence the detectors would need to be roughly 5 mm cubes. Unfortunately, this also increases the detectors cross section for ionizing radiation such as cosmic rays. At aircraft altitudes this can be a serious problem (see Houck and Briotta 1982), so detector dimensions are generally kept small ( $1 \times 1 \times 3$  mm). The detector then must be placed in an integrating chamber to keep the absorption probability high.

Germanium doped with  $\sim 2 \times 10^{14}$   $\text{cm}^{-3}$  of gallium produces acceptor impurity levels  $\sim 10^{-2}$  eV above the valence band. Hence, these detectors are sensitive to FIR shortward of  $\lambda \sim 130$   $\mu\text{m}$ . The application of a uniaxial stress along the [100] crystallographic axis splits the four fold degeneracy at the valence edge in the germanium into two doubly degenerate levels (Price 1961, Hall 1962). The splitting is proportional to the strain amplitude, so that a stress of  $\sim 60$   $\text{kgf/mm}^2$  will bring the upper valence level to within .006 eV of the acceptor level. The result is photodetective response out to  $\sim 205$   $\mu\text{m}$  (Kazanski, Richards and Haller 1977; Haller, Hueschen and Richards 1979).

Stressed Ge:Ga detectors must be kept at very low temperatures to prevent phonon excitation of holes into the acceptor impurity levels. Typical operating temperatures are  $T \sim 2.5^\circ\text{K}$ .

Experience has shown that most of the stress on a stressed detector is due to the differential contraction between the detector housing and the germanium crystal. Thus, the housing should be constructed of a material with a large coefficient of thermal expansion. Aluminum immediately comes to mind. However, housings made of Al have shown a high degree of susceptibility to cold flow, and it may take many thermal cyclings for such a housing to reach a state of equilibrium (Watson 1982). Hard brass appears to be a better candidate for housing material as it shrinks nearly as much as aluminum with decreasing temperature, but is less susceptible to cold flow.

Figure 2.8 shows our design for the detector housing. To minimize cold flow and relaxation of the housing, care has been taken to maximize the cross section of the brass housing through its weakest point. The detector is compressed between two polished stainless steel plugs by a 1/4-28 set screw - ball bearing mechanism. The ball bearing serves to decouple the torque due to the set screw. The integrating cavity is highly polished and is a snug fit for the stainless plugs insuring that the faces of the plugs are perpendicular to the cavity walls and, hence the faces of the Ge:Ga crystal. Stainless steel was chosen as the plug material since it is both very hard and has a small thermal expansion coefficient. This then maximizes the differential contraction between the housing walls and the steel plugs, hence, maximizing the mechanical stress on the cooled detector.

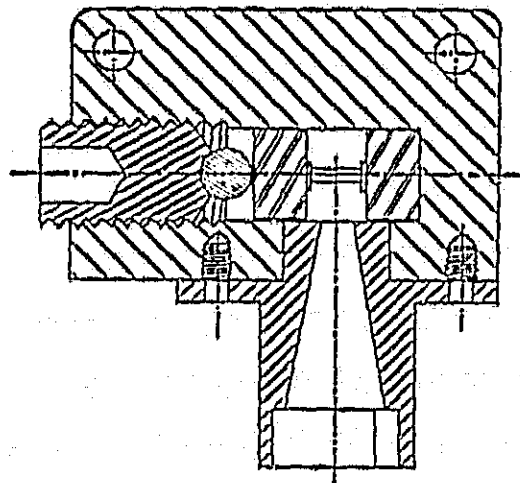
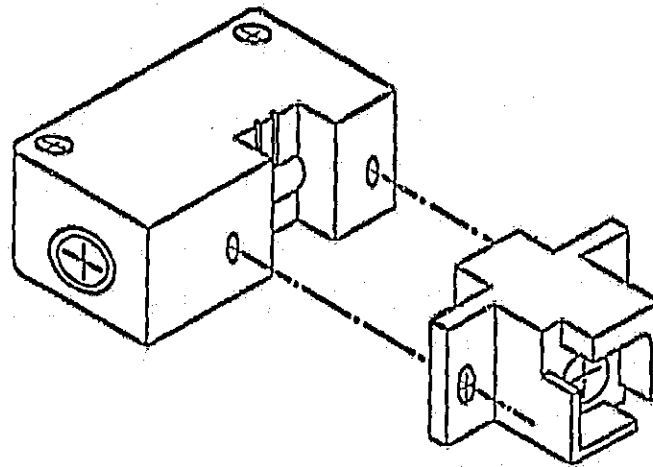


Figure 2.8. Stressed detector housing and cutaway of finished detector. With the light cone removed, detectors are inserted through the cavity behind the light cone. All parts are made of brass save the stainless steel plugs at either end of the detector and the steel ball bearing and set screw.

Detector material was purchased from Eagle-Picher in the form of a 2 3/4 inch diameter wafer cut 3 mm thick along the [100] axis. The germanium had been doped with  $2.1 \times 10^{14}$  cm<sup>-3</sup> of gallium with less than  $10^{13}$  cm<sup>-3</sup> of residual impurities. Ohmic contacts were created as described by Haller, Hueschen and Richards (1979). Both faces of the germanium wafer were successively bombarded with B<sup>+</sup> ions at doses of  $10^{14}$  ions/cm<sup>2</sup> at 25 keV and  $2 \times 10^{14}$  ions/cm<sup>2</sup> at 50 keV. The wafers were next annealed at 200°C in an argon atmosphere to remove implantation damage and to activate the boron. The faces were then sputtered with 500 Å of palladium to serve as a wetting agent and finally a 1 μm layer of gold was sputtered on the faces for electrical contact.

Individual detectors are sliced in 1 mm square sections from the wafer with a diamond wafer saw. The final crystals are 1 mm square by 3 mm long along the [100] axis. The crystals are then etched in a solution of HNO<sub>3</sub>, CH<sub>3</sub>COOH, HF and HBr in the proportion 30:18:18:1 to remove damage done by the diamond saw and any oxidized surface layers. During the etching process, the gold detector contacts must be protected with an overcoat of nail polish which is later removed with acetone.

Electrical contacts to the stressed detector are made through .002" thick soft copper pads which have fine insulated copper wires indium soldered to one corner. These pads are electrically isolated from the detector housings by two layers of cigarette paper. The papers and copper pads are centered, one each, on the stainless steel plugs and held in place with fingernail polish. After the polish sets, excess paper may be scraped away with a razor blade leaving the integrating cavity free of any non-metallic substances (save the detector).

To construct a detector, the stainless steel plugs are first inserted into the integrating cavity via the hole threaded for the set screw. The lead wires are pulled through to come out the entrance aperture. Next, the germanium chip is inserted into the housing through the entrance aperture and centered with a Teflon-restraining jig. Stress is then applied through the set screw - ball bearing assembly. Application of enough stress to lower the detector resistance by 10-15% at room temperature is adequate to produce significant response out to ~ 195  $\mu\text{m}$ . After application of the stress, the Teflon jig may be removed and the light cone mounted. The lead wires are carefully threaded out of the cavity through two tiny (#80 drill) holes. The detector will need to be restressed within a few hours of the initial stressing as the copper pads will cold flow somewhat. After this first restressing, however, the detector will maintain a high level of stress throughout its useful life. (For some as yet unexplained reason, our stressed detectors seem to lose overall response on time scales of the order 6 months - 1 year.) An advantage of these housings is that once detector crystals are cut and etched, a detector may be manufactured within an hour with a minimum of tools. This is an important point when one considers the rigors of shipping our spectrometer across the continent to NASA Ames Research Center. In fact, detectors have been made in the field and flown within a week of manufacture -- though this was an emergency procedure not generally recommended. The manufacture of stressed detectors has been previously described by Watson (1982) and Haller, Hueschen and Richards (1979).

For a more complete discussion on photoconductive devices see Bratt (1977).

## 2.5. Aircraft Environments.

Data presented in this thesis were taken from two of NASA's airborne observatories, the Lear Jet facility and the Kuiper Airborne Observatory (KAO).

### 2.5.1. Lear Jet.

The Lear Jet is by far the smaller of the two facilities. It carries a 30 cm f/6.5 Dall Kirkham Cassegrain telescope mounted in a side port. Due to space considerations, we are not able to mount our interferometer on the Lear Jet telescope and instead fly with just our grating spectrometer. The side looking dewar is mounted directly to the backplate of the telescope which is isolated from aircraft vibrations by an air-bearing and gyroscopically stabilized in flight to an RMS stability of  $\sim .5^{\prime}$  on smooth flights. The air bearing requires that the cabin pressure be only  $\sim 5 \text{ lb/in}^2$  higher than ambient pressure. Hence, the cabin altitude is maintained at  $\sim 14,000$  feet and the experimenters and pilots must wear oxygen masks. The telescope looks out of a side port of the airplane at a relative bearing of  $270^{\circ}$  to the aircraft motion. The air bearing allows  $\sim 6^{\circ}$  play in the telescope pointing in yaw and roll and the telescope may be mechanically cranked to center its window from  $14^{\circ} \sim 28^{\circ}$  in azimuth.

There is room for one experimenter on the aircraft. Unfortunately, data acquisition requires two experimenters. One experimenter, the tracker, sits in the back near the telescope. He operates the tracker rack and performs such tasks as balancing the telescope and cranking the elevation setting screw. He also has the heart-rending task of acquiring the field to be observed with the aid of a bore-sighted guide telescope. This telescope is linked to a video display on the tracker rack through a photomultiplier tube and fiber optics bundle. The zoomed-in tracker field is roughly  $1^\circ$  in azimuth by  $.6^\circ$  in elevation, and the faintest discernible stars are generally  $\sim 9^{\text{th}}$  magnitude on a moonless night. The zoomed out field is approximately ten times larger, and consequently it is difficult to see stars fainter than  $4^{\text{th}}$  magnitude zoomed out. The Lear Jet has automatic tracking ability facilitated by an on-board tracking computer. This computer senses the image of a guide star on the tracking screen and stabilizes that image through feedback to torque motors on the gyroscopes. If there are no guide stars bright enough to be tracked automatically ( $\geq 6^{\text{th}}$  or  $7^{\text{th}}$  magnitude), the observer may manually track with a joystick down to the dimmest visible stars. The chopper throw of the telescope (produced by the oscillating secondary) is variable up to  $14''$ . We typically use as large a throw as possible as our beam sizes are always greater than  $4'' \times 6''$ ;  $6''$  along the direction of the chopper throw. We generally chop at a frequency which gives the best waveform and noise measurements: typically, we chop at 35 Hz. Chopper throw and beam size are determined through observations of point sources such as the planets.

The second observer spends his time running the experimenter's rack, primarily running the data acquisition program on our IMSAI 8080 microcomputer. The data acquisition program was written by Scott D. Smyers and recently revised and updated by Charles E. Fuller at Cornell. Through its use, the IMSAI sends pulses to the drive box which bursts the stepper motor controlling the grating and samples the signals input to the A-D board. The oscillating signals from the spectrometer are synchronously demodulated by a pair of Ithaco lock-in amplifiers. The analog output from the Ithaco's also goes to a strip chart on which the rack operator notes any unusual events (loss of track, high turbulence, etc.) in the data acquisition process.

The optimal data acquisition technique is to make a measurement of a point in the plus beam, then in the minus beam, burst the grating and repeat the process until the entire number of points has been sampled in both beams. This mode, called plus-minus mode, would minimize the effects of temporal fluctuations in sky emissivity. However, nodding the telescope from plus beam to minus beam takes time and frequently results in loss of track on the Lear Jet. In addition, each single beam spectrum generally takes only ~ 90 seconds, so we usually decide to take single beam spectra, alternating minus and plus beams in successive spectra. That is, first a spectral run is taken with the source in the plus beam, then the grating is burst back to the starting position and a spectral run is taken with the source in the minus beam. Spectra generally consist of ~ 12 points sampled, each point separated from the next by ~1/3 resolution element. In this manner, we sample sufficient continuum points about the expected line position to obtain good

calibration, and oversample the line position. The final spectrum, as discussed in Section 2.1 is the difference between the plus and minus beam spectral runs. Each run is recorded onto a floppy disk to be reduced post-flight.

On the best flights up to 39 single beam spectra have been taken -- even while mapping a region. Lear Jet flights are limited to roughly  $2^{\text{h}}10^{\text{m}}$  in duration of which 65-70 minutes are available for astronomical observations. Whenever possible, we take a short (~10 min) leg on a calibrator and the rest of the available time on a source. This both verifies the position of the beams relative to the tracker screen and ensures similar atmospheric conditions for spectra taken on both objects.

The Lear Jet, though a much smaller facility than the KAO offers several advantages that the KAO does not. For extended sources, the smaller telescope size of the Lear Jet does not matter as telescope aperture  $\times$  solid angle product  $A\Omega$  (telescope aperture area  $\times$  beam size) is a constant. Furthermore, the Lear chopper throw is significantly larger than the KAO chopper throw, thus it is much easier to find a blank sky reference when observing extended sources from the Lear Jet.

The Lear telescope may observe closer to the horizon ( $14^\circ$  vs.  $35^\circ$ ) than the KAO. Thus, a larger portion of the sky is available to the Lear observer. One may observe the galactic center from the Lear from the latitude of Ames with no special flight planning. Lear flight series generally consist of 12-16 short ( $2^{\text{h}}10^{\text{m}}$ ) flights while KAO series are generally 2-4 long ( $7^{\text{h}}30^{\text{m}}$ ) flights. Thus, a Lear series allows one much more flexibility in flight planning -- an important

consideration when timing is important as in occultation events (see Chapter 4).

Finally, the Lear Jet typically flies at a somewhat higher altitude than the KAO. Most of the data taking leg of a Lear flight is flown at altitudes between 43,000 and 45,000 feet. While it is true that the KAO may reach 45,000 feet, this flight level may be achieved only after ~ 5 1/2 hours of the flight and 41,000 feet may not be achieved until ~ 2 hrs into a flight. Thus, the Lear Jet will have advantages if the troposphere is high.

#### 2.5.2. KAO.

The KAO is a Lockheed C141A Starlifter which has been modified to carry a 91.5 cm bent Cassegrain telescope. The telescope is isolated from the experimenter area in a cavity located just forward of the wing on the port side of the fuselage. As on the Lear Jet, the telescope is floated on an air bearing and gyrostabilized. However, as the telescope is isolated from the experimenters' area by an ambient pressure cavity, the experimenters may work in a shirt sleeve environment with no oxygen masks. The cavity and telescope are usually pre-cooled prior to takeoff to lower the thermal background.

The KAO contains three on-board computers to control telescope pointing, data acquisition and data processing. NASA flight personnel typically consists of an ADAMS (Airborne Data Acquisition and Management System) operator who oversees KAO computer operations, a tracker operator, who acquires the star field, one or two telescope operators and the

flight director whose primary task is to keep communication channels open between experimenters and all other personnel, especially pilots. There is ample space on board for upwards of six experimenters, though we have generally flown with four or five. Generally, one person runs the data acquisition program, one writes notes on the strip chart and updates the rotation angle, a third reduces data on the EXEC computer, and the fourth "guides" which is to say tweaks the telescope beam to keep it centered in the spectrometer entrance aperture.

The data acquisition program written by Charles Fuller runs on our IMSAI microcomputer which is linked to the ADAMS system through a serial port. The IMSAI controls the pertinent data acquisition commands: bursting the grating and interferometer, sampling the detector signals which have been synchronously demodulated by Ithaco lock-in amplifiers, commanding the tracker computer to nod the telescope through the DATA computer and receiving error flags from the EXEC through the DATA computer. Data sampled by the IMSAI is written on a floppy disk and transferred over to the ADAMS system where it is written on hard disk and magnetic tape. Data reduction is possible in flight using the program M4YAY, written by Scott Smyers. The program runs on the EXEC computer and performs fast Fourier transforms.

KAO flights generally last 7 1/2 hours, of which ~ 6 1/2 hours are available for observations. This is sufficient time to allow observations of ~ six objects including a calibrator. Objects to be observed must be within the 35°-72° window (in elevation) of the telescope. To ensure proper function of the interferometer, we usually observe a source with a strong continuum such as M42 or a planet on our first

leg. With a strong continuum source we single step our interferometer through zero path at two or three different grating positions to verify our preflight zero path position. Actual interferograms generally consist of  $2^n+2$  data points ( $n = 4,5,6$ ) beginning with a sample one burst negative of zero path. For our 5 cm travel stage we have generally used 34 data points which fill a free spectral range large enough to encompass the bandpasses of both detectors. On the KAO, nodding is usually a trivial procedure controlled by the IMSAI through the tracker computer. The nodding procedure employed generally consists of taking the integration at the first interferometer position in the plus beam, nodding and integrating in the minus beam, burst the interferometer to position two, take a minus integration, nod to take a plus integration, burst and so on until we have completed the 34 integrations. Each data point typically consists of the difference between five seconds integrating in the plus beam and five seconds integrating in the minus beam. Including time spent in nodding ( $\sim 1$  sec), pausing for telescope and electronic stabilization ( $\sim 1$  sec) and bursting the interferometer ( $\sim 1$  sec) each 34 point interferogram takes  $\sim 8$  minutes. Upon completion of a forward interferogram, we take a reverse interferogram, beginning at largest travel and bursting back to zero path. During an entire flight over forty interferograms are often taken.

Tracking on a guide star is accomplished by a tracking computer operated by NASA personnel. The tracker is similar to that on the Lear Jet, but much more sensitive, being able to track stars of visual magnitude,  $m_v = 10.5$  to a few arcseconds stability. Use of a dichroic to split the infrared beam from the visible enables us to guide on the

focal plane image. We have made use of an excellent offset guider developed by Prof. James R. Houck to guide on stars as dim as 12<sup>th</sup> magnitude in the focal plane. The offset guider is a twin reticle device which corrects for field rotation by actual rotation of one of the reticles. This movable reticle is placed over a guide star while the fixed reticle denotes the location of the source. The fixed reticle is aligned with the telescope - spectrometer boresight through a pre-flight procedure with a chopped-collimated infrared source. (Referred to as Erickson's source after its inventor, Dr. Edwin F. Erickson of NASA Ames Research Center.) Offsets to the guide star are calculated preflight and dialed into the movable reticle for each object. Keeping the IR source in the entrance aperture is then just a matter of keeping the guide star in the rotating movable reticle. Rotation angles are provided from the housekeeping utilities of the ADAMS system. Focal plane guiding may be practiced on sources as far as  $9''$  from their guide stars. Pointing accuracy may be quite high with such a system, as small as  $\pm 5''$ , while guiding stability is probably of the same order RMS. The plate scale at the focal plane is  $\sim 14''/\text{mm}$  which means the  $4 \times 4$  mm slits in our spectrometer define a square beam roughly  $1'' \times 1''$ .

The chopper throw of the KAO is variable up to  $9''$ . Generally we use a throw just larger than the source extent as nodding takes longer with larger chopper throws (it also takes longer with fainter guide stars) and the chopper is less efficient with larger throws (the time spent between beams is larger for larger throws). The KAO chopper is easily rotated up to  $90^\circ$ , and the centroid of the chopper duty cycle may be varied to minimize the infrared signal from the telescope. As in the

Lear Jet, chopper frequency is chosen to minimize system noise. Generally chopper frequencies of 25 Hz have been used.

### 2.6. Data Acquisition and Reduction.

Data sampling rates and plus-minus reduction are essentially equivalent for the two observatories. We usually integrate for five seconds in each beam for each interferometer or grating position. These five second integrations, called points,  $P_i$ , are subdivided into 35 separate integrations,  $s_n$ , .143 seconds each, each of which is stored on floppy disk. A postflight de-glitching program written by C. Fuller, may be used to remove spikes in the data presumably caused by cosmic rays. They are easily recognized as spikes as they typically last one or two Ithaco time constants (usually set at 125 ms or ~ 1 Hz bandwidth). Generally data is automatically de-glitched by throwing out the five integrations which deviate the most from the mean. This usually results in ~ 20% increase in the signal/noise ratio. The data point for each beam  $P_{i+,-}$  is then given by the average of the  $N$  remaining data points

$$P_{i+,-} = 1/N \sum_{n=1}^N s_n$$

with noise, (standard deviation from the mean), given by

$$\sigma_{i+,-} = \left[ \frac{1}{N} \sum_{n=1}^N (P_{i+,-} - s_n)^2 / (N-1) \right]^{1/2}$$

The final signal for each grating or interferometer position is the difference between the plus and minus beam measurements, so

$$P_i = F_{i+} - P_{i-} ; n_i = ( n_{i+}^2 + n_{i-}^2 )^{1/2}$$

From this point forward, due to the Fourier transform routine required for the KO data, data reduction takes different routes for the two facilities.

### 2.1.1. Star Jet

Grating spectra are averaged with the program AVRG. AVRG presents the user with three options for data reduction. The common denominator for the three is the final noise calculation. In all cases, two noise estimates are made, and the larger of the two is chosen as the noise in the averaged file. If we average N files, each of which contains a measurement  $P_i$  of the source flux at wavelength  $\lambda_i$ , then we define two error estimators

1) Relative mean error -- also known as the standard deviation from the mean:

$$\sigma_{rms} = ( 1/N \sum_{i=1}^N [ (P_S - P_i)^2 / (N-1) ] )^{1/2}$$

2) Mean error -- often termed "internal error":

$$\sigma_{ms} = ( 1/N \sum n_i^2 )^{1/2}$$

If the number of spectra is sufficiently high, ( $\geq 5$ ) then the two error estimates should converge.

These two error estimates apply to a "straight" average of the data, i.e. where each data point is given equal weight (= 1):

$$\bar{P}_S = 1/N \sum_{i=1}^N P_i$$

If one feels that the errors associated with each data point  $P_i$  are reasonable, it is desirable to perform a "weighted" average of the data files, where each data point is weighted by the inverse of the variance:

$$\bar{P}_W = \frac{\sum_{i=1}^N P_i/n_i^2}{\sum_{i=1}^N 1/n_i^2}$$

In this case, the mean error is given by:

$$\sigma_{mW} = \left( \sum 1/n_i^2 \right)^{1/2}$$

The relative mean error is:

$$\sigma_{rW} = \left[ \frac{1}{N(N-1)} \sum (\bar{P}_W - P_i)^2/n_i^2 \div \sum 1/n_i^2 \right]^{1/2}$$

If all of the  $n_i$  are equal, justifying the use of a straight average, then  $\bar{P}_W = \bar{P}_S$ ,  $\sigma_{mW} = \sigma_{mS}$  and  $\sigma_{rW} = \sigma_{rS}$ .

External errors due to guiding, sky fluctuations or instrumental fluctuations may be compensated for through use of the third option of AVRQ; maximum likelihood averaging of files. This technique was suggested by Stephen E. Schneider and has been implemented for much of the Lear data reduction. The essence of the technique is that it acknowledges the existence of external systematic noise in our data, and tries

to maximize the probability that the final average is the correct one through adding a common external error, in quadrature to each data file.

Assuming the  $N$  data points  $P_i$ , for each wavelength  $\lambda_j$  are normally distributed with variance  $n_i^2 + s^2$  where  $n_i$  is our measured noise and  $s$  is the external noise, to be determined, then the likelihood function is given by:

$$L(s) = 1/\sqrt{(2\pi)^N} \prod_{i=1}^N 1/(n_i^2 + s^2)^{1/2} \cdot \exp \left[ -1/2 \sum_{i=1}^N e_i^2 / (n_i^2 + s^2) \right],$$

where  $e_i \equiv P_i - \bar{P}$ , and  $\bar{P} = \bar{P}_W$ , as above. Maximizing with respect to  $s^2$  we have

$$\left. \frac{\partial L}{\partial s^2} \right|_{L_{\max}} = 0 = -1/2 \sum_i 1/(n_i^2 + s^2) + 1/2 \sum_i e_i^2 / (n_i^2 + s^2)^2$$

If we let

$$f(s^2) = \sum_i e_i^2 / (n_i^2 + s^2)^2 - \sum_i 1 / (n_i^2 + s^2) = 0$$

$$\text{then } \partial f(s^2) / \partial s^2 = -2 \sum_i e_i^2 / (n_i^2 + s^2)^3 + \sum_i 1 / (n_i^2 + s^2)^2$$

We may use the Newton-Raphson method to solve for  $s$

$$(s')^2 = s^2 - f(s^2) / [\partial f(s^2) / \partial s^2]$$

and iterate until  $|s' - s| \leq$  an acceptable error.

The maximum likelihood option of AVR<sub>G</sub> makes these calculations to find  $s$  for each wavelength  $\lambda_j$ . The new error for each file is then  $n_j' = (n_j^2 + s^2)^{1/2}$  and averages are calculated as in the weighted average options. The resulting average spectra differ little from weighted averages; means shift a few percent and the final errors are usually slightly smaller, as the relative mean error approaches the mean error.

As mentioned in Section 2.1, spectra are divided by spectra of standard calibrators to remove as much as possible the convolved presence of telluric water vapor features, detector and filter response functions, and beam profile from the source spectrum. Standard calibrators used on Lear Jet flights are the planets Venus, Mars, Saturn and Jupiter, and the Moon. Of the planets, Jupiter and Venus provide the most power, hence the best signal/noise ratios. However, the atmosphere of Jupiter is known to contain deep  $\text{NH}_3$  features, and one must constantly be aware of such features when using Jupiter as a calibrator (see Figure 2.9). The  $J = 2$  and  $J = 3$  rotation-inversion bands of  $\text{NH}_3$  occur in the bandpass of our spectrometer at  $\sim 125$  and  $170 \mu\text{m}$  (see Encrenaz et al. 1971 for details). Venus would be a more suitable candidate, but proximity to the sun prohibits its use much of the time. The Moon might appear to be an ideal calibrator, however its larger angular size means it fills the beam quite differently from the average astronomical source, which diminishes its value as a calibrator.

Calibrator spectra,  $C_j$ , are taken at the same grating position, hence wavelength,  $\lambda_j$ , as the source spectra,  $P_j$ . The resulting spectrum  $s_j$  is then

$$s_j = P_j/C_j$$

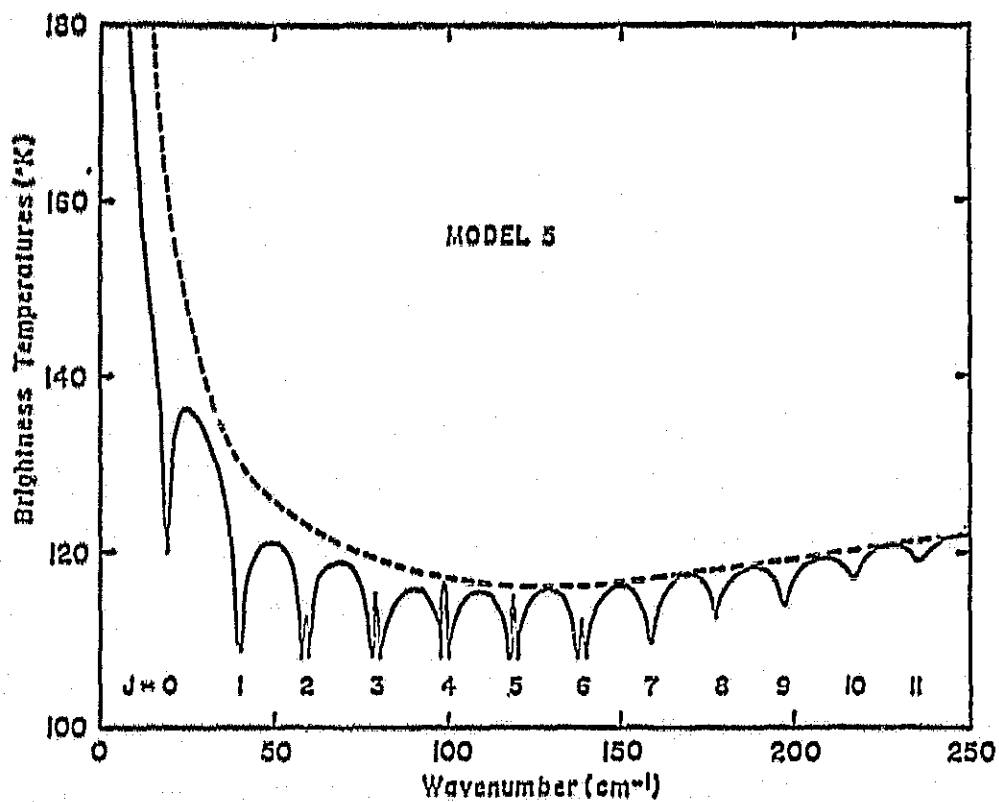


Figure 2.9. Theoretical far-infrared spectrum of Jupiter from Encrenaz et al. 1971. The  $J = 2$  ( $\sim 170\mu\text{m}$ ) and  $J = 3$  ( $\sim 125\mu\text{m}$ ) pure rotational bands of  $\text{NH}_3$  are within the spectral range of our spectrometer and must be avoided when using Jupiter as a calibrator.

with associated noise  $\sigma_1 = s_1 (\sigma_C^2/C_1^2 + n_1^2/P_1^2)^{1/2}$ . Absolute flux calibration follows from the known physical parameters of the calibrator.

Dividing of spectra is accomplished by the program LINFIT. LINFIT also allows one to calculate the flux in an emission or absorption feature by fitting a weighted least squares Gaussian plus polynomial to the divided spectrum. Baseline curvature is usually entirely removed through the dividing of spectra, so the polynomial is usually first order.

If one knows the precise location of an expected line in low signal/noise ratio data, one may recover some information from the data through the binning option of LINFIT. Since we oversample our data, data, usually three samples/resolution element, we may average, or bin, these three elements into one number. This final number generally has a S/N ratio  $\sqrt{3}$  times better than the individual samples, resulting in the recovery of useful data from a noisy spectrum. Binning may be achieved through a straight or weighted average, as above.

### 2.6.2. KAO.

The data acquisition program written by Charles E. Fuller performs in-flight plus-minus reduction on the KAO. This plus-minus reduced file is transferred to the EXEC via the DATA computer. The data file is accessible to the program, M4YAY, written by S. Smyers which allows the experimenter to perform a first cut data reduction in flight. The fast

Fourier transform routine for M4YAY was developed by B. Langdon and S. Sande at Princeton University, from the approach of Cooley and Tukey (1965). In-flight data reduction is an invaluable aid, as it enables us to estimate when we have integrated sufficiently on a line and may move on to the next feature.

The KAO data is de-glitched prior to post-flight plus-minus reduction, using the individual integrations stored on floppy disks during flight. The Fourier transform program which runs on the IMSAI, again written by S. Smyers, is similar to the in-flight program. The program reconstructs wavelengths from the burst size, step size and grating central wavelength as in Section 2.3.3 above. The Fourier transform routine calculates both the cosine and sine transforms. As reflected data are symmetric about zero path, all the sine components are zero. Averages are performed in the standard way, with each interferogram being transformed first and resultant spectra averaged with equal weight, i.e.

$$s_j = 1/N \sum_{i=1}^N s_{ij} \quad ; \quad n_j = \left[ 1/N \sum_{i=1}^N (s_{ij} - s_j)^2 / (N-1) \right]^{1/2}$$

where  $s_j$  = average of the  $N$  data points  $s_{ij}$  each with error  $n_{ij}$ .

The noise  $n_j$  is just the standard deviation from the mean.

With our 5 cm travel stage, walkoff has been a chronic problem. As mentioned in section 2.3.5 above, this "droopy shoulder" appearance may be minimized by fitting a line to the data and raising the wings. In addition, our Fourier transform programs allow one to apodize the data

with spectral lag windows. These windows smoothly apodize the data from a weight of one at zero path to a weight of zero at largest path. This effectively eliminates the discontinuity at largest path and results in a higher signal to noise ratio in the transformed spectrum at the expense of system resolution. When apodization is necessary we have generally used the Bartlett (triangle) window which weights the data according to:

$$w_i = 1 - i/N$$

where  $i$  denotes the data point as measured from the zeroth data point (zero path) and  $N$  is the total number of bursts (= # data points - 1). The CO spectra of Figures 2.1 and 2.4 are apodized data with droopy shoulders removed. For a complete discussion of spectral lag windows, see Jenkins and Watts (1968). For a complete discussion of the fast Fourier transform see Bergland (1969). A discussion of Fourier transform spectrometers and interferogram sampling error correction techniques may be found in Möller and Rothshild (1971).

## CHAPTER 3

### FINE STRUCTURE LINES AND RADIATIVE TRANSFER

#### 3.1. Introduction.

This chapter is split into two sections. The first section discusses the physics of fine structure transitions and radiative transfer, while the second section briefly discusses some of the processes which compete with fine structure lines to cool the interstellar medium.

Fine structure levels occur in any atomic or ionic species with valence electrons. The two species of concern in this work, CII and OI, have one and four equivalent 2p electrons respectively. The resulting  $2p^1$  and  $2p^4$  configurations are ordered by the residual electrostatic interaction into terms which differ in total orbital angular momentum  $L \equiv \sum l_i$  and total spin angular momentum of the electrons  $S \equiv \sum s_i$ . We have denoted by  $l_i$  the orbital angular momentum, ( $|l_i| = 1$ ), and by  $s_i$  the spin angular momentum ( $|s_i| = 1/2$ ) of each 2p electron. For CII there is only one 2p electron resulting in the single term  $^2P$ . The superscript denotes the number of levels of which the term is composed, and equals  $2S+1$ . The letter P denotes the total orbital angular momentum of the term and follows the usual convention S,P,D,F, ... referring to terms of  $L = 0,1,2,3,\dots$ . The  $^2P$  term is further split

by the spin-orbit (L·S coupling) interaction into the levels  ${}^2P_{3/2}$ ;  ${}^2P_{1/2}$  where the subscript denotes  $J \equiv L + S$ . Each level,  $J$ , has a degeneracy  $g_J$  given by  $g_J = 2J+1$ . The 157  $\mu\text{m}$  [CII] fine structure line results from radiative transitions from the  ${}^2P_{3/2}$  level to the  ${}^2P_{1/2}$  ground state.

The  $2p^4$  configuration of OI is split into the three terms  ${}^1S$ ,  ${}^1D$ , and  ${}^3P$ . The lowest lying term is that with the highest spin (Hund's rule), the  ${}^3P$  term. This triplet is split into the levels  ${}^3P_0$ ,  ${}^3P_1$  and  ${}^3P_2$ . As the  $2p$  shell is more than half full, the levels are inverted, with the level of largest  $J$ ,  ${}^3P_2$ , being the ground state. Figure 3.1 shows the OI level diagram. The  ${}^1S$  and  ${}^1D$  levels are metastable, the forbidden transitions to the  ${}^3P$  term resulting in the familiar nebular lines at  $\sim 6300 \text{ \AA}$  and  $\sim 2972 \text{ \AA}$ . These levels have excitation temperatures  $\geq 20,000^\circ\text{K}$  and are thus negligibly excited in the low temperature ( $T \sim$  a few hundred  $^\circ\text{K}$ ) regions where the FIR fine structure lines dominate the cooling. The 145.53  $\mu\text{m}$  line arises from radiative transitions from the  ${}^3P_0 \sim {}^3P_1$  level while the 63.17  $\mu\text{m}$  line occurs through transitions from the  ${}^3P_1$  level to the  ${}^3P_2$  ground state.

Fine structure lines occur between levels in a configuration. The fine structure lines of concern in this work occur between levels within a term and as such involve no change in the spatial wavefunction of the electronic state, but rather changes in  $J$ , i.e., the vector addition of the  $S$  and  $L$  vectors. As such, these transitions are forbidden to electric dipole radiation. Magnetic dipole transitions are allowed and hence the excited fine structure levels are metastable with lifetimes  $\sim$  days.

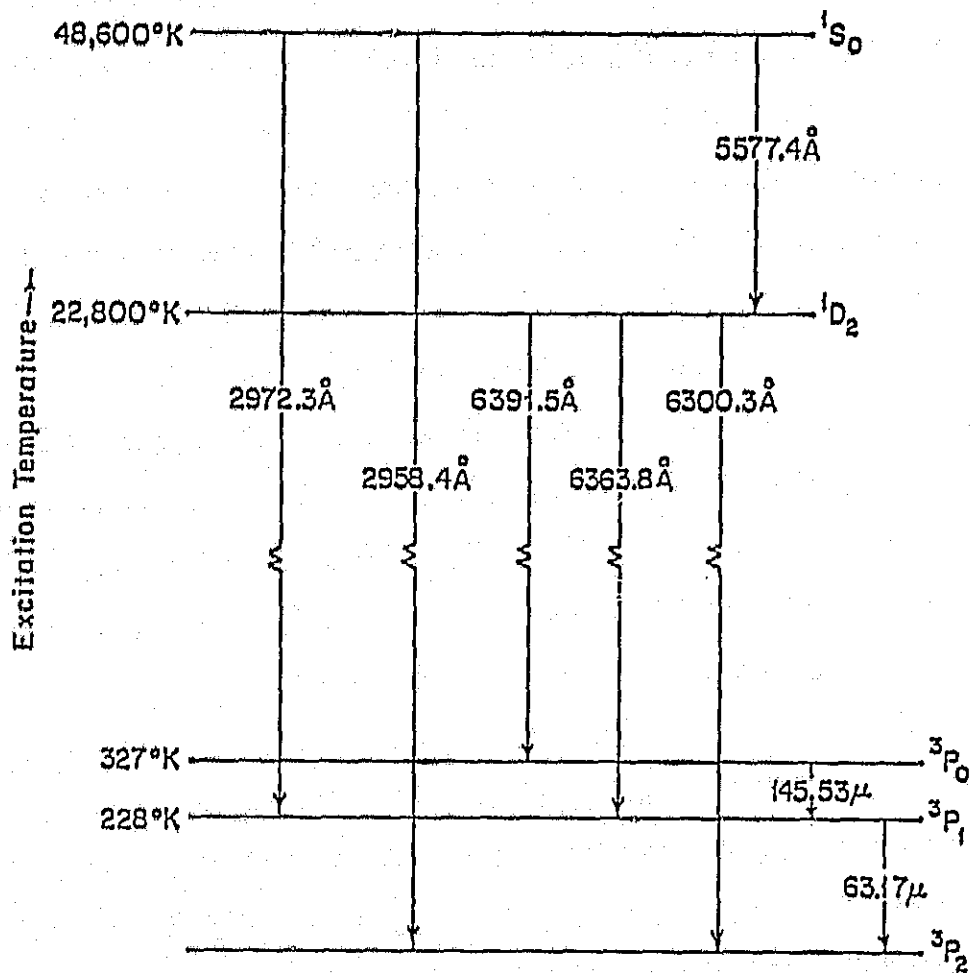


Figure 3.1. Energy levels for the  $(1s)^2(2s)^2(2p)^4$  configuration of neutral oxygen. Wavelengths for the visible and ultraviolet lines are taken from Osterbrock, 1974.

Much may be learned from the study of FIR fine structure lines. As we show in section 3.3 below, fine structure lines, particularly the 157  $\mu\text{m}$  [CII] line dominate the cooling of gas at temperatures below a few thousand degrees. In section 3.2, we show that the measurement of one FIR fine structure line together with a priori knowledge of the number density of exciting particles,  $n_c$  (such as from radio measurements) allows one to determine the relative abundance of the emitting species. The ratio of the two [OI] fine structure line intensities enables one to determine  $n_c$  in a model-independent way. The importance of far infrared and submillimeter fine structure lines has been the subject of several reviews in the recent literature including: Simpson (1975), Kafatos and Lynch (1980), Watson and Storey (1980), and Harwit (1984).

### 3.2. Radiative Transfer.

#### 3.2.1. Equation of Transfer.

The fundamental equation governing macroscopic radiative processes in regions as diverse as stellar interiors and diffuse interstellar clouds is the equation of transfer:

$$dI_\nu/ds = -\alpha_\nu I_\nu + j_\nu \quad [3.1]$$

where  $I_\nu$  [ $\text{erg s}^{-1} \text{cm}^{-2} \text{sr}^{-1} \text{Hz}^{-1}$ ] is the specific intensity of the beam along a pathlength  $s$  [cm], and  $\alpha_\nu$  [ $\text{cm}^{-1}$ ] and  $j_\nu$  [ $\text{erg s}^{-1} \text{sr}^{-1} \text{cm}^{-3} \text{Hz}^{-1}$ ] are the monochromatic absorption and emission coefficients. This equation fully describes the macroscopic behavior of radiation in a medium which both absorbs and emits radiation. The measured quantity,  $I_\nu$ , allows us to determine the physical properties  $\alpha_\nu$  and  $j_\nu$  of

the medium. The primary task for this section is to determine forms for these two coefficients, and hence solve 3.1. Much of the formalism we use in this discussion follows Rybicki and Lightman (1979) and Spitzer (1978).

In principle, when  $\alpha_\nu$  and  $j_\nu$  are known it is easy to solve the equation of transfer. Unfortunately, scattering is also present in a real medium thus complicating the analysis. We postpone the discussion of scattering to section 3.2.4.

Equation 3.1 is readily solved in two limiting cases:

1 -- Emission only,  $\alpha = 0$ . If  $I_\nu(0)$  is the background intensity incident upon an emitting slab of thickness  $s$ , then the emergent intensity  $I_\nu$  is given by

$$I_\nu = \int_0^s j_\nu(s') ds' + I_\nu(0)$$

2 -- Absorption only,  $j_\nu = 0$ . Let  $I_\nu(0)$  again be the intensity incident upon our absorbing slab of thickness  $s$ , then the intensity will be attenuated in the medium so that the emergent intensity is given by:

$$I_\nu = I_\nu(0) \exp\left(-\int_0^s \alpha_\nu(s') ds'\right)$$

One defines the optical depth,  $\tau_\nu$ , by

$$d\tau_\nu = \alpha_\nu ds + \tau_\nu(s) = \int_0^s \alpha_\nu(s') ds'. \quad [3.2]$$

Hence, in case 2,

$$I_\nu = I_\nu(0) e^{-\tau_\nu}$$

From the exponential form of the above equation, it is clear that the average photon will travel to (at least) an optical depth  $\tau_\nu$  with probability  $e^{-\tau_\nu}$ . Thus, the average optical depth traversed by a photon,  $\langle \tau_\nu \rangle$ , is unity.

$$\langle \tau_\nu \rangle \equiv \int_0^{\infty} \tau_\nu e^{-\tau_\nu} d\tau_\nu = 1$$

We may define the mean free path of a photon,  $\lambda_\nu$ , in a homogeneous medium by  $\langle \tau_\nu \rangle = \langle \alpha_\nu \lambda_\nu \rangle = 1 \implies \lambda_\nu = 1/\alpha_\nu$ . A medium is said to be optically thin if the average photon escapes the medium without absorption, i.e.,  $\tau_\nu < 1$ . If  $\tau_\nu > 1$ , the medium is optically thick. Dividing 3.1 by  $\alpha_\nu$  we may rewrite the equation of transfer in terms of the source function,  $S_\nu \equiv j_\nu/\alpha_\nu$  and optical depth  $\tau_\nu$ :

$$\frac{dI_\nu}{d\tau_\nu} = -I_\nu + S_\nu$$

This leads us to the formal solution of the equation of transfer:

$$I_\nu(\tau_\nu) = I_\nu(0)e^{-\tau_\nu} + \int_0^{\tau_\nu} e^{-(\tau_\nu - \tau_\nu')} S_\nu(\tau_\nu') d\tau_\nu' \quad [3.3]$$

If the source function is constant in the medium, we may integrate to yield

$$I_\nu(\tau_\nu) = S_\nu + e^{-\tau_\nu}(I_\nu(0) - S_\nu)$$

Note: As  $\tau_\nu \rightarrow \infty$ ,  $I_\nu \rightarrow S_\nu$ . Also note that in thermodynamic equilibrium, we must have  $j_\nu = \alpha_\nu B_\nu$  (Kirchoff's law) where  $B_\nu$  is the Planck blackbody function given by

$$B_{\nu} = \frac{2h\nu^3}{c^2} (e^{h\nu/kT} - 1)^{-1}$$

Thus if a system is thermalized at some temperature  $T$ , the source function reduces to the Planck function.

### 3.2.2. Einstein Coefficients and Detailed Balance.

Einstein first realized that Kirchoff's law implies a relationship between the emission and absorption of radiation on the atomic level. This relationship is expressed through the Einstein coefficients.

Let us begin by limiting our attention to a two level quantum system, denoted by  $u$  (upper) and  $l$  (lower). The difference in energy between the levels is  $\Delta E_{ul} = h\nu_{ul}$ . We define  $A_{ul}$  as the spontaneous decay rate through emission of a photon when the system makes a spontaneous transition from level  $u$  to  $l$ . In addition, a passing photon of energy  $h\nu_{ul}$  may be absorbed by the system in the ground state  $l$  and excite the atom to the excited level  $u$ . If we denote  $J_{\nu} = 1/4\pi \int_{4\pi} I_{\nu} d\Omega$  as the mean intensity of the photon field, then the probability,  $P_a$ , of a photon being absorbed per unit time is given by

$$P_a = B_{lu} \int_0^{\infty} J_{\nu} \phi(\nu) d\nu$$

where  $B_{lu}$  is the Einstein coefficient for absorption and  $\phi(\nu)$  is the

line profile, which in general is strongly peaked about  $\nu_{u1}$  and is normalized by  $\int_0^{\infty} \phi(\nu) d\nu = 1$ .

If the system is in the excited state, then the photon field may stimulate emission of a photon. The Einstein coefficient for stimulated emission  $B_{u1}$  is defined such that the probability,  $P_s$ , per unit time of the emission of a photon through stimulated emission is:

$$P_s = B_{u1} \int_0^{\infty} J_{\nu} \phi(\nu) d\nu$$

For individual atoms, the line profiles may be approximated by a Lorentz profile:

$$\phi(\nu) = \frac{\gamma/4\pi^2}{(\nu - \nu_{u1})^2 + (\gamma/4\pi)^2}$$

where  $\gamma$  is the natural line width, related by the uncertainty principle to the Einstein A coefficient for the transition by  $\gamma \sim A_{u1}$ . For the lines of interest in this work,  $A_{u1} \sim 10^{-4} - 10^{-6} \text{ s}^{-1}$ . At reasonable astrophysical temperatures ( $T \geq 10^4 \text{ K}$ ), Doppler line widths are  $\Delta\nu_{\text{Dop}} \geq 10^6 - 10^7 \text{ Hz}$  for these lines -- much greater than the natural line widths. Therefore, the mean intensity  $J_{\nu}$  is constant over the natural line profile, and we may take  $J_{\nu}$  out of the integral above. Evaluating  $J_{\nu}$  at the line center, we have:

$$P_s = B_{u1} J_{\nu_{u1}} \quad [3.4]$$

The Einstein coefficients are related at the atomic level (the system need not be in thermodynamic equilibrium) by:

$$B_{1u} = g_u/g_l B_{u1} \quad [3.5]$$

$$B_{u1} = \frac{c^2}{2h\nu_{u1}^3} A_{u1} \quad [3.6]$$

The absorption and emission coefficients may thus be written in terms of the Einstein coefficients:

$$\alpha_\nu = h\nu/4\pi (n_l B_{1u} - n_u B_{u1}) \phi(\nu) \quad [3.7]$$

$$j_\nu = h\nu/4\pi (n_u A_{u1}) \phi(\nu) \quad [3.8]$$

Stimulated emission has been included as negative absorption since stimulated emission and absorption both are dependent on the local photon field.

Rewriting the equation of transfer 3.1 in terms of the Einstein coefficients we have:

$$\frac{dI_\nu}{ds} = \frac{-h\nu}{4\pi} (n_l B_{1u} - n_u B_{u1}) \phi(\nu) I_\nu + \frac{h\nu}{4\pi} n_u A_{u1} \phi(\nu) \quad [3.9]$$

We divide 3.9 by  $\alpha_\nu$  and integrate to obtain:

$$I_\nu = \int_0^s \frac{h\nu}{4\pi} \phi(\nu) n_u A_{u1} e^{-\tau_\nu} ds \quad [3.10]$$

Most far-infrared fine structure lines are optically thin ( $\tau_\nu \ll 1$ ).

For these lines, we may immediately integrate 3.10 to yield:

$$I = \int_0^\infty I_\nu d\nu = \frac{h\nu}{4\pi} N_u A_{u1} = \frac{h\nu}{4\pi} \frac{n_u}{n_l} N_l A_{u1} \quad [3.11]$$

Thus our measured parameter, the intensity in the line integrated over the line profile,  $I$ , determines the column density  $N_u \equiv n_u s$  of the emitting species in the excited state  $u$ . To determine the total column density,  $N_I$  of the emitting species, we must determine the relative level populations  $n_u/n_I$ . We turn our attention to an atomic system with arbitrary number of energy levels  $m$ .

In local thermodynamic equilibrium (LTE), levels are populated according to the Boltzmann distribution:

$$n_j/n_I = g_j/f e^{-E_j/kT} \quad [3.12]$$

where  $g_j$  is the statistical weight of level  $j$  which has an excitation energy  $E_j$  above the  $j=0$  ground state.  $n_j/n_I$  is the ratio of the number density of level  $j$  to the total number density of the species  $n_I$ .  $f$  is the partition function defined by:

$$f = \sum_{k=0}^m g_k e^{-E_k/kT}$$

LTE is maintained only when collisional processes dominate radiative processes in determining the level populations. In the interstellar medium, where number densities are quite small, collisional excitation rates for fine structure levels are often comparable to radiative transition rates. Thus, the fine structure levels are rarely populated in accordance with the Boltzmann distribution. For a steady state system, we may determine the relative level populations through the principle of detailed balance: the number of transitions into a level  $j$  per unit time must equal the number of transitions out of that level per unit time.

Levels are populated and depopulated through both collisional and radiative processes. For a steady state, the net change in the population of a level  $j$  per unit time is zero,  $dn_j/dt = 0$ . Equating transitions into a level  $j$  to those out of the level  $j$  we have:

$$\begin{aligned} & \sum_{k \neq j} n_k (n_c \gamma_{kj} + B_{kj} J_{\nu_{kj}}) + \sum_{k > j} n_k A_{kj} \\ & = n_j \left( \sum_{k \neq j} (n_c \gamma_{jk} + B_{jk} J_{\nu_{kj}}) + \sum_{k < j} A_{jk} \right) \end{aligned} \quad [3.13]$$

Equation 3.13 is subject to the constraint that  $\sum n_j = n_I$  -- the sum of the populations of the levels equals the total population of the emitting species. In 3.13 above,  $n_k A_{kj}$  ( $n_j A_{jk}$ ) are the spontaneous decay rates into (out of) the level  $j$ , and  $n_k B_{kj} J_{\nu_{kj}}$  ( $n_j B_{jk} J_{\nu_{jk}}$ ) are the absorption and stimulated emission rates into (out of) the level  $j$ .  $J_{\nu_{kj}}$  is the mean intensity of the radiation field at the line center frequency  $\nu_{kj}$ . The collisional excitation rate into the level  $j$  is defined by  $n_c \gamma_{kj}$  [ $\text{sec}^{-1}$ ] where again  $n_c$  = number density of collisionally exciting particles (electrons, protons, hydrogen atoms or hydrogen molecules), and  $\gamma_{kj}$  is the rate coefficient for collisional excitation of level  $j$ . The rate coefficient for collisional de-population of level  $j$ ,  $\gamma_{jk}$  is related to  $\gamma_{kj}$  by:

$$\gamma_{jk} = g_k/g_j \gamma_{kj} e^{-E_{jk}/kT}$$

where  $E_{jk} \equiv E_k - E_j$ .

Rate coefficients are defined as the mean value of the transition probability per unit time for excitation of a level averaged over a

Maxwellian velocity distribution for exciting particles. The collisional excitation rate is given by  $\gamma_{jk} = \langle v_e \sigma_{jk} \rangle$  where  $\sigma_{jk}$  is the excitation cross section,  $v_e$  is the velocity of the exciting particles and the brackets denote the velocity average. For electronic excitation of ionic species, the cross section may be written in a particularly useful form by defining a "collision strength"  $\Omega(j,k)$ :

$$\sigma_{jk} = \pi/g_j [h/(2\pi m_e v_e)]^2 \Omega(j,k)$$

where  $m_e$  = electron mass. Collision strengths are calculated quantum mechanically and are fairly constant with temperature above the threshold energy for collisional excitation of the ion. For the fine-structure transitions of interest in this thesis, the electron temperature in ionized regions is always much greater than the excitation threshold. Collision strengths may be shown to be symmetric,  $\Omega(k,j) = \Omega(j,k)$  and are related to the rate coefficients by:

$$\gamma_{kj} = \frac{h^2 \Omega(j,k)}{g_k (2\pi m_e)^{3/2} (kT)^{1/2}}$$

Thus above threshold, the rate coefficients for electronic excitation of ionic species are proportional to  $T^{-1/2}$ .

Collisional cross sections,  $\sigma_{kj}$ , tend to be constant for low energy collisions between neutral particles, such as HI - OI collisions. Collision strengths thus vary as  $T$  resulting in rate coefficients proportional to  $T^{+1/2}$ . Rate coefficients must thus be tabulated as a function of temperature.

Table 5.2

## Observations

Region	Transition	Intensity ( $\text{erg s}^{-1}\text{cm}^{-2}\text{sr}^{-1}$ )	Comments
Broadbeam ( $4'' \times 6''$ )	[OI] $^3P_0 - ^3P_1$ (145.53 $\mu\text{m}$ )	$2.2 \pm 0.4 \times 10^{-3}$	This work normalized from $7'' \times 7''$ beam.
	[OI] $^3P_1 - ^3P_2$ (63.17 $\mu\text{m}$ )	$3.0 \times 10^{-2}$	Estimate from contour map of Furniss et al. (1983).
	[CII] $^2P_{3/2} - ^2P_{1/2}$ (157.73 $\mu\text{m}$ )	$3.8 \pm 1.1 \times 10^{-3}$	Kurtz et al. (1983).
Trapezium ( $1'' \times 1''$ )	[OI] $^3P_0 - ^3P_1$ (145.53 $\mu\text{m}$ )	$5.7 \pm 1.7 \times 10^{-3}$	This work.
	[OI] $^3P_1 - ^3P_2$ (63.17 $\mu\text{m}$ )	$6.2 \pm 0.6 \times 10^{-2}$	Werner et al. (1982) ( $45''$ circular beam).

### 5.4.1. Ionization Fronts.

The 63  $\mu\text{m}$  intensity expected from an ionization front of thickness  $D$  and number density of electrons,  $n_e$  is given by equation 3.19:

$$I = \frac{j_{63}}{n_e n_{\text{OI}}} (n_e^2 D) \epsilon_{\text{OI}} \frac{n_0}{n_{\text{H}}}$$

In this equation, and for the discussion which follows we use gaseous oxygen and carbon abundances as determined for the inner regions (within  $2^{\circ}$  of the Trapezium) by Peimbert (1982):  $\epsilon_{\text{O}} n_{\text{O}}/n_{\text{H}} = 4.7 \times 10^{-4}$ ;  $\epsilon_{\text{C}} n_{\text{C}}/n_{\text{H}} = 3.7 \times 10^{-4}$ .

The thickness of the ionization front is likely to be of the order of the mean free path of a Lyman  $\alpha$  photon,  $D \sim 10^{17}/n_{\text{H}}$  cm. If we assume pressure equilibrium between the D-type ionization front (cf. Spitzer 1978) and the inner regions of the Orion Nebula [ $n_e \sim 4500 \text{ cm}^{-3}$ ;  $T_e \sim 8900^{\circ}\text{K}$  (Peimbert 1982)], 50% ionization and an electron temperature  $T_e \sim 6000^{\circ}\text{K}$  in the ionization front, then:

$$I \sim 4 \times 10^{-6} \text{ erg s}^{-1} \text{ cm}^{-2} \text{ sr}^{-1}$$

where we have used Figure 3.7 for  $j_{63}/(n_e n_{\text{OI}})$ . This is four orders of magnitude smaller than the observed [OI] intensities. We conclude that the observed [OI] emission does not arise in the ionization front.

### 5.4.2. Warm Neutral Regions.

[OI] transitions may also be excited through collisions with neutral hydrogen atoms in the dense CII regions just beyond the ionization front. (See Chapter 4 for a discussion of CII regions.) We begin our discussion by first restricting ourselves to our broad-beam ( $4^{\circ} \times 6^{\circ}$  emitting region) measurements.

#### 5.4.2.1. Broadbeam models.

CII regions typically have temperatures of the order  $300^{\circ}\text{K}$ . In pressure equilibrium, the CII region would thus have a number density of HI atoms  $n_{\text{HI}} \sim 3 \times 10^5 \text{ cm}^{-3}$ . For such temperatures and pressures, we would expect a line ratio,  $I_{63}/I_{145} \sim 40$  (Fig. 3.8). However, the observed intensity ratio for our broadbeam measurements is  $\sim 18$ . This means the 63  $\mu\text{m}$  radiation must be self-absorbed.

To reproduce the observed 63  $\mu\text{m}$  intensity, the minimum column density of neutral oxygen in an emitting region of temperature  $T \sim 300^{\circ}\text{K}$  and density  $n_{\text{H}} \sim 3 \times 10^5 \text{ cm}^{-3}$  is given by equation 3.19:

$$N_{\text{OI}} = \frac{I_{63}}{(j_{63}/n_{\text{H}}n_{\text{OI}})n_{\text{H}}} \sim 1.6 \times 10^{18} \text{ cm}^{-2}$$

The line center optical depth is given by eq. 3.22 in equation 3.24:

$$\tau_{63} \sim \frac{\epsilon_{63}^{1/2} \lambda^3 A_{63}}{\Delta \nu_D 8\pi^{3/2}} \left( \frac{g_1}{g_2} N_2 - N_1 \right) \quad [5.1]$$

where  $N_2$  and  $N_1$  are the column densities of oxygen atoms in levels  $J=2$  and  $J=1$ ,  $\epsilon_{63}$  is the probability per absorption of collisional de-excitation of the  $J=1$  level,  $g_J$  are the statistical weights of level  $J$ , and  $\Delta\nu_D$  is the Doppler width of the  $63 \mu\text{m}$  line. For  $T = 300^\circ\text{K}$  and  $n_{\text{HI}} \sim 3 \times 10^5 \text{ cm}^{-3}$ ,  $\epsilon_{63} \sim .38$  (equations 3.26 and 3.27). Using Figure 3.4 we estimate the relative level populations:  $n_1/n_2 \sim .052$ ,  $n_0/n_2 \sim .019$ . Thus  $N_2 \sim .93 N_{\text{OI}}$ ,  $N_1 \sim .052 N_{\text{OI}}$ , and we have:

$$\tau_{63} \sim \frac{3 \times 10^5}{\Delta\nu_D}$$

Jaffe and Pankonin (1978) have measured the C109 $\alpha$  and C137 $\beta$  radio recombination lines from carbon atoms in the dense CII regions just beyond the ionization front. They measure a line width (FWHM)  $\sim 4 \text{ km s}^{-1}$ , corresponding to a Doppler width,  $\Delta\nu_D$  (see equation 3.23), of  $2.4 \text{ km s}^{-1}$ . If we assume that this is the width of FIR lines emerging from the dense CII regions, the  $63 \mu\text{m}$  line must have an optical depth  $\tau_{63} \geq 1.2$ . We construct models for the [OI] emitting CII regions with self-absorption of the  $63 \mu\text{m}$  radiation in mind.

Radial velocities of the carbon recombination lines led Jaffe and Pankonin to model the emission as arising from three distinct dense CII regions, distinguished by their radial velocities. The low velocity ( $v_{\text{LSR}} \sim 6 \text{ km s}^{-1}$ ) CII region lies in front of the HII region in the dark bay. The middle velocity region ( $v_{\text{LSR}} \sim 8.5 \text{ km s}^{-1}$ ) is thought to be a sheet of material viewed edge-on which lies at the interface between the HII region and M43 to the northeast. The highest velocity

$v_{LSR} \sim 11 \text{ km s}^{-1}$ ) CII region lies behind the Trapezium at the interface between the HII region and the molecular cloud. The half-power distribution of these CII regions is  $\sim 7^{\circ}$  (R.A.)  $\times 5^{\circ}$  (Dec.) in extent -- centered roughly  $2^{\circ}$  north of the Trapezium. Thus the CII regions coincided reasonably well with the observed [OI] emission.

Kurtz et al. (1983) have observed the  $157 \mu\text{m}$  [CII] line emission from these CII regions using an earlier version of our grating spectrometer. In their  $4^{\circ} \times 7^{\circ}$  beam centered on the FIR continuum peak, they measure a line intensity  $I_{157} \sim 3.8 \times 10^{-3} \text{ erg s}^{-1} \text{ cm}^{-2} \text{ sr}^{-1}$ . Assuming the  $145 \mu\text{m}$  [OI] line and the  $157 \mu\text{m}$  [CII] lines arise in the same regions, we may use the ratio of the line intensities (assuming both lines are optically thin) to determine the temperature of the emitting regions. Figure 5.3 displays the ratio of the reduced emissivities of the two lines:

$$R \equiv \frac{\left( \frac{j_{145}}{n_{\text{OI}} n_{\text{HI}}} \frac{n_{\text{O}}}{n_{\text{H}}} \right)}{\left( \frac{j_{157}}{n_{\text{CII}} n_{\text{HI}}} \frac{n_{\text{C}}}{n_{\text{H}}} \right)}$$

as a function of density for various temperatures of interest. The cosmic abundance terms above ( $n_{\text{O}}/n_{\text{H}} = 4.5 \times 10^{-4}$ ;  $n_{\text{C}}/n_{\text{H}} = 3.7 \times 10^{-4}$ ) normalize the emissivities to emissivity per hydrogen atom.

Also plotted in Figure 5.3 is the locus of points determined by the requirement that there be pressure equilibrium between the compact HII region and the CII fronts. It can be seen that the  $145 \mu\text{m}$  to  $157 \mu\text{m}$  line ratio is a sensitive temperature indicator in the density regions of interest. The ratio of the measured  $145 \mu\text{m}$  intensity to the  $157 \mu\text{m}$

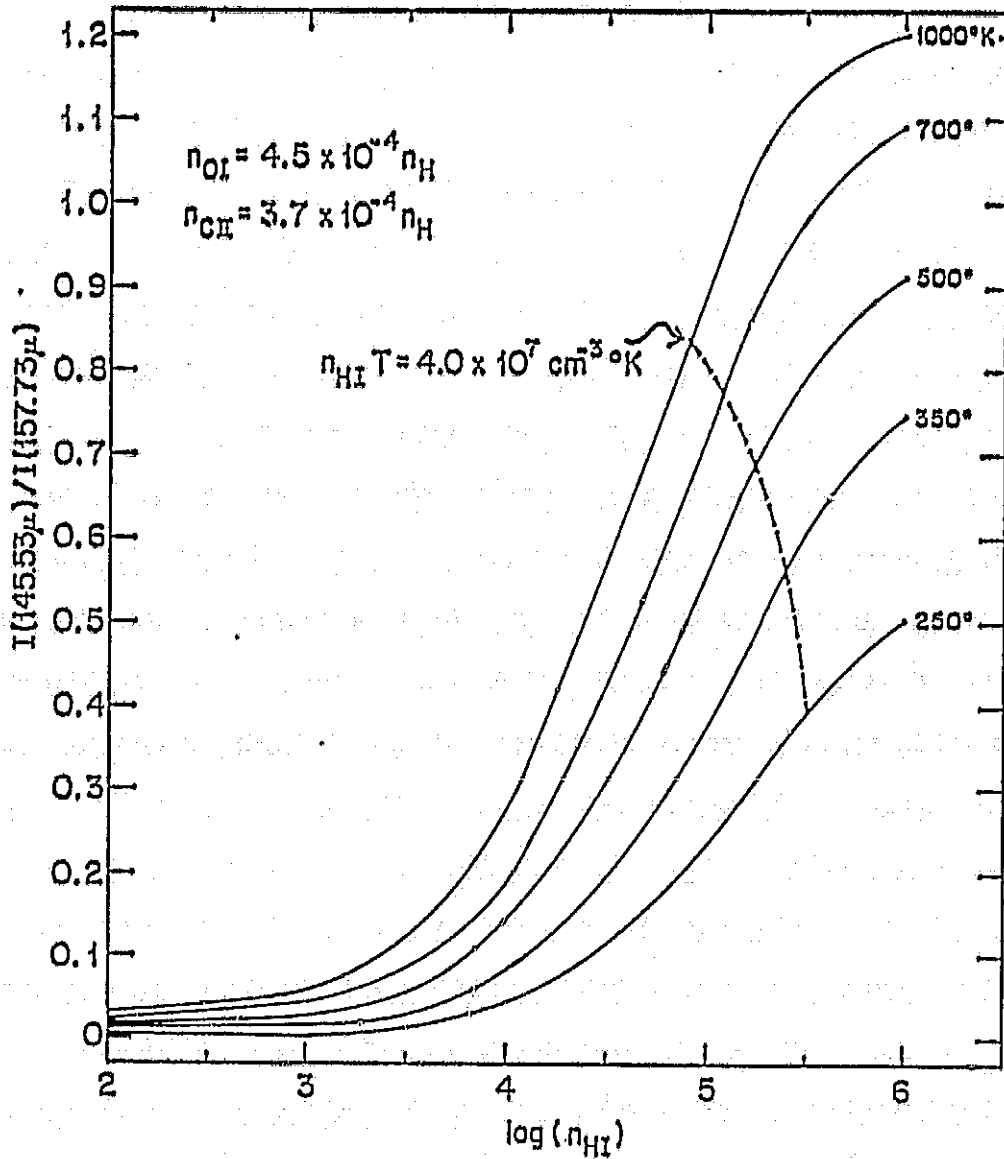


Figure 5.3. The ratio of the 145.53 $\mu\text{m}$  [OI] to 157.74 $\mu\text{m}$  [CII] line intensities as a function of  $n_{\text{HI}}$ . We have assumed abundances of oxygen and ionized carbon as given by Peimbert, 1982. The dotted line crossing the temperature contours depicts solutions which correspond to pressure equilibrium for the CII region and the ionized gas.

intensity is:

$$R = \frac{I_{145}}{I_{157}} = 0.58$$

Using Figure 5.3 we determine  $T \sim 350^\circ\text{K}$ ,  $n_{\text{H}} \sim 2.3 \times 10^5 \text{ cm}^{-3}$  for the emitting regions.

From equation 3.19, we calculate the average line of sight column density of [OI] emitting material:

$$N_{\text{HI}} = \frac{I_{145}}{(j_{145}/n_{\text{OI}}n_{\text{HI}}) n_{\text{O}}/n_{\text{H}} (n_{\text{HI}})} = 7.3 \times 10^{21} \text{ cm}^{-2}$$

where we have used Figure 3.6 to determine  $j_{145}/n_{\text{OI}}n_{\text{HI}}$  for  $T = 350^\circ\text{K}$  and  $n_{\text{HI}} = 2.3 \times 10^5 \text{ cm}^{-3}$ . This column density is within the range of models for CII regions (see section 4.3.2.1).

Using equation 3.22 in equation 3.24, we calculate the line center optical depth of the 145  $\mu\text{m}$  line:

$$\tau_{145} = \frac{\epsilon_{145} \lambda^3 A_{145}}{\Delta\nu 8\pi^{3/2}} \left( \frac{g_0}{g_1} N_1 - N_0 \right)$$

$\epsilon_{145}$  may be calculated from equations 3.28 in equation 3.29, evaluating  $J_\nu$  with equation 3.44:

$$\epsilon_{145} \sim .76$$

Using Figure 3.4 to obtain the relative level populations we have:

$$\tau_{145} \sim .04$$

In a completely analogous manner, we calculate  $\epsilon_{157} \sim .98$ ,  $n_{3/2}/n_{1/2} \sim 1.55$ ,  $N_{3/2} \sim 1.62 \times 10^{18} \text{ cm}^{-2}$ ,  $N_{1/2} \sim 1.08 \times 10^{18} \text{ cm}^{-2}$ , so that  $\tau_{157} \sim .34$ . Thus both lines are optically thin, and we are justified in using their ratio to determine the temperature of the emitting regions.

As argued above, the 63  $\mu\text{m}$  radiation must be self-absorbed. To estimate the 63  $\mu\text{m}$  intensity from the CII regions, we must refer to the analysis of optically thick lines given in Section 3.2.5 above.

The intensity of the 63  $\mu\text{m}$  line as related to the Planck blackbody function,  $B_\nu$  is given by equation 3.43:

$$I_{63} = I_\nu \Delta\nu = B_\nu \Delta\nu \left[ 1 + \alpha \frac{(1-e^\beta)}{(e^\beta - e^{-\beta})} - \alpha^{-1} \frac{(1-e^{-\beta})}{(e^\beta - e^{-\beta})} \right] \quad [5.2]$$

where  $B_\nu$  is the Planck blackbody formula,  $\alpha \equiv (1-\sqrt{\epsilon})/(1+\sqrt{\epsilon})$  and  $\beta \equiv \sqrt{3} \epsilon \tau_{63}$ , and  $\Delta\nu$  [Hz] is the line width, full width half maximum. Having solved for  $T$  and  $n_{\text{HI}}$  above,  $\epsilon_{63}$  is determined. Using equations 3.27 and 3.44 in 3.26, for  $I_{63} = .030 \text{ erg s}^{-1} \text{ cm}^{-2} \text{ sr}^{-1}$ , we obtain  $\epsilon_{63} = .38$ . The only free parameter in 5.2 above is  $\tau_{63}$ , the line center optical depth, given by equation 5.1. Using Figure 3.4 to find the relative level populations at  $T = 350^\circ\text{K}$ ,  $n_{\text{HI}} = 2.3 \times 10^5 \text{ cm}^{-3}$  we have:

$$\tau_{63} \sim \frac{3.9}{\Delta\nu_D}$$

where  $\Delta\nu_D$  is expressed in  $\text{km s}^{-1}$  and we have used  $N_{0I} = 4.5 \times 10^{-4} N_{\text{HI}}$ ;  $N_{\text{HI}} = 7.3 \times 10^{21} \text{ cm}^{-2}$ . To produce the observed 63  $\mu\text{m}$  intensity ( $I_{63} = .030 \text{ erg s}^{-1} \text{ cm}^{-2} \text{ sr}^{-1}$ ) we require  $\tau_{63} = 2.0$ . The Doppler width of the line is then  $\Delta\nu_D = 1.9 \text{ km s}^{-1}$ , or a line width (FWHM) of

$$\Delta v = 3.2 \text{ km s}^{-1}$$

This line width is somewhat smaller than, but consistent with the C109 $\alpha$  recombination line widths measured by Jaffe and Pankonin. Their measured line widths range from 1.7-7.6 km s $^{-1}$  with an average line width of 3.9 $\pm$ 1.2 km s $^{-1}$ . Thus, the [OI] lines most probably arise from HI impact excitation of OI in the carbon recombination line emitting CII region.

#### 5.4.2.2. Trapezium region model.

To model the enhanced emission from the Trapezium region, we must first subtract the contribution due to the broadbeam model. This leaves us with [OI] intensities:

$$I_{63} = .032 \quad ; \quad I_{145} = 3.5 \pm 1.7 \times 10^{-3} \text{ erg s}^{-1} \text{ cm}^{-2} \text{ sr}^{-1}$$

The optical sodium D line work of Isobe (1980) and the bidimensional photometry of Laques and Vidal (1979) reveal the presence of globules, i.e. neutral gas condensations embedded within the Trapezium cluster. These globules could be remnants of the original molecular cloud from which the Trapezium stars formed [evaporation timescales  $\sim 3 \times 10^4$  years, consistent with the age of the cluster (Vidal, 1982)] or might have formed from elephant trunk intrusions of neutral gas into the HII region, à la Pottasch (1965).

Each globule (typical diameters  $\leq .002$  pc) will have an associated

CII front enveloping it, in much the same way CII regions envelop GMC's in the galactic plane (Chapter 4). In many cases the carbon will be ionized throughout the globule -- then the entire neutral region becomes a good source of [OI] emission.

If we assume the conditions in these CII regions to be similar to those from which our broadbeam emission arises ( $T \sim 350^\circ\text{K}$ ,  $n_{\text{HI}} \sim 2.3 \times 10^5 \text{ cm}^{-3}$ ) and take a line width of  $\sim 4 \text{ km s}^{-1}$ , then the measured  $63 \mu\text{m}$  intensity requires a line center optical depth  $\tau_{63} \sim 2.0$ . This corresponds to a column density of atomic hydrogen in the [OI] emitting regions of the order  $N_{\text{HI}} \sim 10^{22} \text{ cm}^{-2}$ . The optically thin  $145 \mu\text{m}$  intensity is then:

$$I_{145} = 3.0 \times 10^{-3} \text{ erg s}^{-1} \text{ cm}^{-2} \text{ sr}^{-1}$$

This is smaller than the observed intensity but well within the measurement errors.

We thus require roughly one globule along a typical line of sight in the Trapezium to explain the observed emission. This is consistent with the conclusions of Isobe (1980). The extra CII region in the Trapezium would also give rise to enhanced carbon recombination line emission, which is also measured. Our results are summarized in Table 5.3.

Table 5.3

Model:

Region	T (°K)	$n_{\text{HI}}$ ( $\text{cm}^{-3}$ )	$N_{\text{HI}}$ ( $\text{cm}^{-2}$ )	$\Delta V_{\text{FHM}}$ ( $\text{km s}^{-1}$ )	Line Intensity ( $\text{erg s}^{-1} \text{cm}^{-2} \text{sr}^{-1}$ )	Line Center Optical Depth
Broadbeam $4^{\circ} \times 6^{\circ}$	350	$2.3 \times 10^5$	$7.3 \times 10^{21}$	3.2	[OI]	2.9
					63 $\mu\text{m}$ : $3.0 \times 10^{-2}$	0.05
					145 $\mu\text{m}$ : $2.2 \times 10^{-3}$	
Trapezium $1^{\circ} \times 1^{\circ}$	350	$2.3 \times 10^5$	$9 \times 10^{21}$	4.0	[OII]	2.0
					63 $\mu\text{m}$ : $3.2 \times 10^{-2}$	0.05
					145 $\mu\text{m}$ : $3.0 \times 10^{-3}$	

### 5.5. Summary.

We have made the first astronomical detections of the 145.53  $\mu\text{m}$  [OI] line through observations of the Orion Nebula. By comparing observations of the  $^3P_1 - ^3P_0$  (157.74  $\mu\text{m}$ ) transition of CII we are able to deduce that these three emission lines all arise in dense CII regions at the interfaces between the ionized gas and molecular cloud in Orion. Using the 145.53  $\mu\text{m}$  to 157.73  $\mu\text{m}$  line intensity ratios, we are able to determine that these regions are at a temperature  $T \sim 350^\circ\text{K}$  with number density of hydrogen atoms  $n_{\text{H I}} \sim 2.3 \times 10^5 \text{ cm}^{-3}$ . We show that the 63.17  $\mu\text{m}$  [OI] line is self-absorbed with line center optical depth  $\tau_{63} \sim 2.0$ . This is the first such determination of an optically thick FIR fine structure line.

APPENDIX

Selected Far Infrared Fine Structure Transitions ( $\lambda \geq 20 \mu\text{m}$ )  
(After Schmid-Burgk, 1982)

Transition	Species	Excitation Potential <sup>a</sup> (eV)	Ionization Potential <sup>a</sup> (eV)	Wavelength (microns)	First Astronomical Observation
$2p_{3/2} - 2p_{1/2}$	BI	---	8.298	655.57	----
	CII	11.260	24.383	157.737 $\pm$ .002 <sup>b</sup>	Russell et al. (1980)
	NIII	29.601	47.448	57.343 $\pm$ .003	Moorwood et al. (1980b)
	OIV	54.934	77.412	25.87 $\pm$ .02	Forrest, McCarthy, and Houck (1980)
	AlI	---	5.986	89.237 $\pm$ .0025	----
	SIII	8.151	16.345	34.814	----
	PIII	19.725	30.18	17.885 $\pm$ .007	----
$2p_{1/2} - 2p_{3/2}$	FI	---	17.422	24.745 $\pm$ .001	----

Transition	Species	Excitation Potential <sup>a</sup> (eV)	Ionization Potential <sup>a</sup> (eV)	Wavelength (microns)	First Astronomical Observation
$3p_2-3p_1,$ $3p_1-3p_0$	CI	---	11.260	370.414±.0015 609.133±.001	Jaffe et al. (1984) Phillips et al. (1980)
	NII	14.534	29.601	121.7 ±.27 203.5 ±.8	---- ----
	OIII	35.116	54.934	51.816±.003 88.355±.008	MeInick et al. (1978) Ward et al. (1975)
	FIV	62.707	87.138	25.83 44.25	---- ----
	NeV	97.11	126.21	14.32 24.28 ±.02	---- Forrest, McCarthy, and Houck (1980)
	SiII	---	8.151	68.473 129.68	---- ----
	PII	10.486	19.725	32.87 60.68	---- ----
	SIII	23.33	34.83	18.7129 ±.0004 33.456±.001	Baluteau et al. (1976) Moorwood et al. (1980a)
	ClIV	39.61	53.46	11.76 ±.01 20.38 ±.02	---- ----

Transition	Species	Excitation Potential <sup>a</sup> (eV)	Ionization Potential <sup>a</sup> (eV)	Wavelength (microns)	First Astronomical Observation	
$^3p_0-^3p_1,$ $^3p_1-^3p_2$	O I	---	13.618	145.52547 $\pm .000085$ 63.17000 $\pm .00003$	Stacey et al. (1983a) MeInick et al. (1979)	
	Fe II	17.422	34.970	67.16 29.33	----- -----	
	Ne III	40.962	63.45	36.02 15.55	Shure et al. (1984) Pottasch et al. (1984)	
	Na IV	71.64	98.91	21.29 9.039	----- -----	
	Si	---	10.360	56.309 $\pm .01$ 25.2490 $\pm .0003$	----- -----	
	C III	12.967	23.81	33.281 14.368	----- -----	
	Ar III	27.629	40.74	21.84 $\pm .1$ 8.9910 $\pm .0002$	Shure et al. (1984a) <sup>c</sup> Gillett, Forrest, and Merrill (1973)	
	$^5D_3-^5D_4$	Fe I	---	7.870	24.04	-----
Fe III		16.18	30.651	22.93	-----	
$^5D_2-^5D_3$		Fe I			34.71	-----
		Fe III			33.04	-----
$^5D_1-^5D_2$	Fe I			54.31	-----	
	Fe III			51.68	-----	
$^5D_0-^5D_1$	Fe I			111.18	-----	
	Fe III			105.4	-----	

Transition	Species	Excitation Potential <sup>a</sup> (eV)	Ionization Potential <sup>a</sup> (eV)	Wavelength (microns)	First Astronomical Observation
${}^6D_{7/2} - {}^6D_{5/2}$	FeII	7.870	16.18	25.99	----
${}^6D_{5/2} - {}^6D_{3/2}$				35.352	----
${}^6D_{3/2} - {}^6D_{1/2}$				51.28	----
${}^6D_{1/2} - {}^6D_{3/2}$				87.41	----
${}^5D_4 - {}^5D_3$	FeV	54.8	75.0	20.79	----
${}^5D_3 - {}^5D_2$				25.97	----
${}^5D_2 - {}^5D_1$				36.50	----
${}^5D_1 - {}^5D_0$				68.97	----

<sup>a</sup> From Lang (1980).

Excitation Potential  $\equiv$  Energy needed to form the species.

Ionization Potential  $\equiv$  Energy needed to ionize the species.

<sup>b</sup> Crawford et al. (1985).

<sup>c</sup> Possible detection.

## REFERENCES

Allen, C.W. (1976) Astrophysical Quantities, 3rd Ed. (London: Athlone Press).

Altenhoff, W.J., Downes, D., Goad, L., Maxwell, A., and Rinehart, R. (1970) Astron. Astrophys. Suppl. Ser. 1, 319.

Armstrong, K.R., and Low, F.J. (1973) Appl. Opt. 12, 2007.

Bahcall, J.N., and Wolf, R.A. (1968) Astrophys. J. 152, 701.

Baluteau, J.-P., Bussoletti, E., Anderegg, M., Moorwood, A.F.M., and Coron, N. (1976) Astrophys. J. 210, L45.

Barlow, M.J., and Silk, J. (1976) Astrophys. J. 207, 131.

Bergland, G.D. (1969) IEEE Spectrum 6, 41.

Blitz, L., Fich, M., and Kulkarni, S. (1983) Science 220, 1233.

Boyd, R.W. (1982) Infrared Phys. 22, 157.

Bratt, P.R. (1977) In Semiconductors and Semimetals, R.K. Willardson and A.C. Beer, Eds. (New York: Academic Press), Vol. 12, p. 39.

Burton, W.B., and Gordon, M.A. (1978) Annu. Rev. Astron. Astrophys. 14, 275.

Burton, W.B., Gordon, M.A., Bania, T.M., and Lockman, F.J. (1975) Astrophys. J. 202, 30.

Cooly, J.W., and Tukey, J.W. (1965) Math. Comput. 19, 297.

Cravens, T.E., and Dalgarno, A. (1978) Astrophys. J. 219, 750.

Crawford, M.K., Genzel, R., Townes, C.H., and Watson, D.H. (1985) Submitted to Astrophys. J.

Dalgarno, A., and McCray, R. (1972) Annu. Rev. Astron. Astrophys. 10, 375.

deJong, T., Dalgarno, A., and Boland, W. (1980) Astron. Astrophys. 91, 68.

Downes, D., Wilson, T.L., Beiging, J., and Wink, J. (1980) Astron. Astrophys. Suppl. Ser. 40, 379.

Draine, B.T. (1978) Astrophys. J. Suppl. Ser. 36, 595.

Encrenaz, Th., Gautier, D., Vapillon, L., and Verdet, J.P. (1971)

Astron. Astrophys. 11, 431.

Fellgett, P.B. (1951) Doctoral Thesis, Cambridge University, Cambridge, England.

Flower, D.R., Launay, J.M., and Roueff, E. (1977) In Les Spectres des Molecules Simples au Laboratoire et en Astrophysique (Liège: Université de Liège Institut a' Astrophysique), p. 137.

Forrest, W.J., McCarthy, J.F., and Houck, J.R. (1980) Astrophys. J. 240, L37.

Furniss, I., Jennings, R.E., King, K.J., Lightfoot, J.F., Emery, R.J., Fitton, B., and Naylo, D.A. (1983) Mon. Not. R. Astron. Soc. 202, 859.

Gatley, I., Becklin, E.E., Sellgren, K., and Werner, M.W. (1979) Astrophys. J. 233, 575.

Genzel, R., Reid, M.J., Moran, J.M., Downes, D., and Ho, P.T.P. (1982) In "Symposium on the Orion Nebula to Honor Henry Draper", Ann. N.Y. Acad. Sci. 395, 142.

Gerola, H., and Glassgold, A.E. (1978) Astrophys. J. Suppl. Ser. 37, 1.

Gillett, F.C., Derenjak, E.L., and Joyce, R.R. (1977) Opt. Eng. 16, 544.

Gillett, F.C., Forrest, W.J., and Merrill, K.M. (1973) Astrophys. J. 183, 87.

Gispert, R., Puget, J.L., and Serra, G. (1982) Astron. Astrophys. 106, 293.

Glassgold, A.E., Huggins, P.J., and Schucking, E.L., Eds. (1982) "Symposium on the Orion Nebula to Honor Henry Draper", Ann. N.Y. Acad. Sci. 395.

Glassgold, A.E. and Langer, W.D. (1973) Astrophys. J. 186, 859.

Goldsmith, P.F. and Langer, W.D. (1978) Astrophys. J. 222, 881.

Hall, J.J. (1962) Phys. Rev. 128, 68.

Haller, E.E., Hueschen, M.R., and Richards, P.L. (1979) Appl. Phys. Lett. 34, 495.

Harding, D.S., and Harding, A.K. (1982) Astrophys. J. 257, 603.

Hart, L. and Pedlar, A. (1976) Mon. Not. R. Astron. Soc. 176, 547.

Harwit, M. (1984) In Galactic and Extragalactic Infrared Spectroscopy (Dordrecht: D. Reidel), p. 145.

Harwit, M., Kurtz, N.T., Russell, R.W., and Smyers, S. (1981) Appl. Opt. 20, 3792.

Harwit, M. and Sloan, N.J.A. (1979) Hadamard Transform Optics (New York: Academic Press).

Hayes, M.A. and Nussbaumer, H. (1984) Astron. Astrophys. 134, 193.

Henderson, A.P., Jackson, P.D., and Kerr, F.J. (1982) Astrophys. J. 263, 116.

Herter, T., Briotta, D.A. Jr., Gull, G.E., Shure, M.A., and Houck, J.R. (1982) Astrophys. J. 259, L109.

Houck, J.R. and Briotta, D.A. Jr. (1982) Infrared Phys. 22, 215.

Houck, J.R. and Ward, D.B. (1979) Publ. Astron. Soc. Pac. 91, 140.

Isobe, S. (1980) Publ. Astron. Soc. Jpn. 32, 423.

Jaffe, D.T., Harris, A.I., Silber, M., Genzel, R., and Betz, A.L. (1985) "Detection of the  $370 \mu\text{m } ^3\text{P}_2\text{-}^3\text{P}_1$  Fine-Structure Line of CI." Submitted to Astrophys. J. (Letters).

Jaffe, D.T. and Pankonin, V. (1978) Astrophys. J. 226, 869.

Jenkins, E.B. (1978) Astrophys. J. 220, 107.

Jenkins, G.M., and Watts, D.G. (1968) Spectral Analysis and its Applications (San Francisco: Holden-Day).

Johnson, H.M. (1968) In Nebulae and Interstellar Matter, B.M. Middlehurst and L.H. Aller, Eds. (Chicago: Univ. Chicago Press), p. 65.

Kafatos, M., and Lynch, J.P. (1980) Astrophys. J. Suppl. Ser. 42, 611.

Kazanskii, A.G., Richards, P.L., and Haller, E.E. (1977) Appl. Phys. Lett. 31, 496.

Keyes, R.J., and Quist, T.M. (1970) In Semiconductors and Semimetals, Vol. 5 (New York: Academic Press), p. 321.

Krügel, E., Thum, C., Martin-Pintado, J., and Pankonin, V. (1982) Astron. Astrophys. Suppl. Ser. 48, 345.

Kulkarni, S.R., Blitz, L., and Heiles, C. (1982) Astrophys. J. 259, L63.

Kurtz, N.T., Smyers, S.D., Russell, R.W., Harwit, M., and Melnick, G. (1983) Astrophys. J. 264, 538.

Lang, K.R. (1980) Astrophysical Formulae, 2nd Ed. (New York: Springer-Verlag).

Langer, W. (1976) Astrophys. J. 206, 699.

Laques, P. and Vidal, J.-L. (1979) Astron. Astrophys. 73, 97.

Launay, J.M. and Roueff, E. (1977) J. Phys. B 10, 879.

Leung, C.M. (1975) Astrophys. J. 199, 340.

McCarthy, D.E. (1967) J. Opt. Soc. Am. 57, 699.

McKee, C.F. and Ostriker, J.P. (1977) Astrophys. J. 218, 148.

Melnick, G., Gull, G.E., Harwit, M., and Ward, D.B. (1978) Astrophys. J. 222, L137.

Melnick, G., Gull, G.E., and Harwit, M. (1979) Astrophys. J. 227, L29.

Melnick, G.J. (1981) Ph.D. Dissertation, Cornell University, Ithaca, NY.

Melnick, G.J., Stacey, G.J., Viscuso, P.J., and Fuller, C.F. (1985)

"Observations of the 157.7 m [CII] Emission from the Galactic HII

Regions W3 and W51." Submitted to Astrophys. J.

Mendell, W.W. and Low, F.J. (1970) J. Geophys. Res. 75, 3319.

Mendoza, C. (1983) In Planetary Nebulae, D.R. Flower, Ed. (IAU Symp.

#103), Ch. 4, p. 143.

Mezger, P.G. (1978) Astron. Astrophys. 70, 565.

Mezger, P.G. (1984) In Galactic and Extragalactic Infrared Spectroscopy (Dordrecht: D. Reidel), p. 423.

Mirabeli, I.F. and Morras, R. (1984) Astrophys. J. 279, 86.

Möller, K.D., and Rothschild, W.G. (1971) Far-Infrared Spectroscopy (New York: Wiley-Interscience).

Moorwood, A.F.M., Baluteau, J.-P., Anderegg, M., Coron, N., Biraud, Y., and Fitton, B. (1980a) Astrophys. J. 238, 565.

Moorwood, A.F.M., Salinari, P., Furniss, I., Jennings, R.E., and King, K.J. (1980b) Astron. Astrophys. 90, 304.

Morton, D.C. (1975) Astrophys. J. 197, 85.

Morton, D.C. (1978) Astrophys. J. 222, 863.

Nishimura, T., Low, F.J., and Kurtz, R.F. (1980) Astrophys. J. 239, L101.

Osterbrock, D.E. (1974) Astrophysics of Gaseous Nebulae (San Francisco: Freeman).

Papoulis, A. (1977) Signal Analysis (New York: McGraw-Hill).

Peimbert, M. (1982) In "Symposium on the Orion Nebula to Honor Henry Draper", Ann. N.Y. Acad. Sci. 395, 24.

Phillips, T.G., Huggins, P.J., Kuiper, T.B.H., and Miller, R.E. (1980) Astrophys. J. 238, L103.

Pottasch, S.R. (1965) Vistas Astron. 6, 149.

Pottasch, S.R., Beintema, D.A., Raimond, E., Baud, B., van Duinen, R., Habing, H.J., Houck, J.R., deJong, T., Jennings, R.E., Olmon, F.H., and Wesselius, P.R. (1984) Astrophys. J. 278, L33.

Pottasch, S.R., Wesselius, P.R., and van Duinen, R.J. (1979) Astron. Astrophys. 74, L15.

Price, P.J. (1961) Phys. Rev. 124, 713.

Rybicki, G.B. and Lightman, A.P. (1979) Radiative Processes in Astrophysics (New York: Wiley and Sons).

Russell, R.W., Melnick, G., Gull, G.E., and Harwit, M. (1980) Astrophys. J. 240, L99.

Russell, R.W., Melnick, G., Smyers, S.D., Kurtz, N.T., Gosnell, T.R., Harwit, M., and Werner, M.W. (1981) Astrophys. J. 250, L35.

Salpeter, E.E. (1979) In The Large Scale Characteristics of the Galaxy (IAU Symp. #84), p. 245.

Sanders, D.B. (1981) Doctoral Thesis, State Univ. of New York (Stony Brook), p. 140.

Sanders, D.B., Solomon, P.M., and Scoville, N.Z. (1984) Astrophys. J. 276, 182.

Sanders, D.B., Clemens, D.P., Scoville, N.Z., and Solomon, P.M. (1984a) "The Massachusetts-Stony Brook CO Survey", to appear in Astrophys. J. Suppl. Ser.

Saraph, H.E. (1973) J. Phys. B 6, L243.

Schmid-Burgk, J. (1982) In Numerical Data and Functional Relationships (New Series), Group VI, Vol. 2c, H.H. Landolt and R. Bornstein, Eds. (Springer-Verlag: Berlin), p. 116.

Schmidt, M. (1957) Bull. Astron. Inst. Neth. 13, 247.

Schraml, J. and Mezger, P.G. (1969) Astrophys. J. 156, 269.

Scoville, N.Z. and Solomon, P.M. (1975) Astrophys. J. 199, L105.

Shure, M.A., Houck, J.R., Gull, G.E., and Herter, T. (1984) Astrophys. J. 281, L29.

Shure, M.A., Houck, J.R., Herter, T., Gull, G.E., and Graf, P. (1984a)  
"Mid-Infrared Spectroscopy of Planetary Nebula", in proceedings of:  
"NASA/A.S.P. Symposium on Airborne Astronomy", NASA/Ames Research  
Center, Moffett Field, CA.

Silk, J. (1973) Ann. Rev. Astron. Astrophys. 11, 269.

Simpson, J.A. (1975) Astron. Astrophys. 39, 43.

Solomon, P.M. and Sanders, D.B. (1980) in Giant Molecular Clouds in the Galaxy, P.M. Solomon and M.G. Edmunds, Eds. (New York: Pergamon), p. 65.

Spitzer, L., Jr. (1978) Physical Processes in the Interstellar Medium  
(New York: Wiley and Sons).

Spitzer, L., Jr. and Tomasko, M.G. (1968) Astrophys. J. 152, 971.

Stacey, G.J., Kurtz, N.T., Smyers, S.D., Harwit, M., Russell, R.W., and  
Melnick, G. (1982) Astrophys. J. 257, L37.

Stacey, G.J., Kurtz, N.T., Smyers, S.D., and Harwit, M. (1983) Mon.  
Not. R. Astron. Soc. 202, 25P.

Stacey, G.J., Smyers, S.D., Kurtz, N.T., and Harwit, M. (1983a)  
Astrophys. J. 265, L7.

Stacey, G.J., Smyers, S.D., Kurtz, N.T., and Harwit, M. (1983b)

Astrophys. J. 268, L99.

Stacey, G.J., Viscuso, P.J., Fuller, C.E., and Harwit, M. (1985)

Astrophys. J. 289 (in press).

Stephens, T.L. and Dalgarno, A. (1973) Astrophys. J. 186, 165.

Storey, J.W.V., Watson, D.M., and Townes, C.H. (1979) Astrophys. J.

233, 109.

Strong, A.W., Riley, P.A., Osborne, J.L., and Murray, J.D. (1982)

Mon. Not. R. Astron. Soc. 201, 495.

Tielens, A.G.G.M., and Hollenbach, D. (1985) "Photodissociation

Regions: I. Basic Model". Submitted to Astrophys. J.

Tielens, A.G.G.M., and Hollenbach, D. (1985a) "Photodissociation

Regions: II. A Model for the Orion Photodissociation Region".

Submitted to Astrophys. J.

Todd, T.R., Clayton, C.M., Telfair, W.B., McCubbin, T.K., Jr., and

Pliva, J. (1976) J. Molec. Spectrosc. 63, 201.

Traub, W.A. and Stier, M.T. (1976) Appl. Opt. 15, 364.

Tucker, K.D., Kutner, M.L., and Thaddeus, P. (1973) Astrophys. J.  
186, L13.

Vidal, J.-L. (1982) in "Symposium on the Orion Nebula to Honor Henry  
Draper", Ann. N.Y. Acad. Sci. 395, 176.

Viscuso, P.J., Stacey, G.J., Fuller, C.E., Kurtz, N.T., and Harwit, M.  
(1985) "Submillimeter Observations of OH and CH in Orion", submitted to  
Astrophys. J.

Walmsley, C.M. (1975) In HII Regions and Related Topics, T.L. Wilson and  
D. Downes, Eds. (New York: Springer-Verlag), p. 17.

Ward, D.B., Dennison, B., Gull, G., and Harwit, M. (1975) Astrophys.  
J. 202, L31.

Watson, D.M. (1982) Ph.D. Dissertation, Univ. California, Berkeley, CA.

Watson, D.M., and Storey, J.W.V. (1980) Int. J. Infrared Millimeter  
Waves 1, 609.

Watson, W.D. (1972) Astrophys. J. 176, 103.

Werner, M.W. (1970) Astrophys. Lett. 6, 81.

Werner, M.W. (1982) In "Symposium on the Orion Nebula to Honor Henry  
Draper", Ann. N.Y. Acad. Sci. 395, 79.

Werner, M.W., Dinnerstein, H.L., Hollenback, D.J., Lester, D.F., Genzel, R., Watson, D.M., and Storey, J.W.V. (1982) Bull. Am. Astron. Soc. 14, 610.

Werner, M.W., Gatley, I., Harper, D.A., Becklin, E.E., Lowenstein, R.F., Telesco, C.M., and Thronson, H.A. (1976) Astrophys. J. 204, 420.

Westerhout, G. (1957) Bull. Astron. Inst. Neth. 13, 201.

Westerhout, G. (1958) Bull. Astron. Inst. Neth. 14, 215.

Wright, E.L. (1976) Astrophys. J. 210, 250.

Wynn-Williams, C.G., Genzel, R., Becklin, E.E., and Downes, D. (1984) Astrophys. J. 281, 172.

York, D.G., Spitzer, L., Bohlin, R.C., Hill, J., Jenkins, E.B., Savage, B.D., and Snow, T.P. (1983) Astrophys. J. 266, L55.